Pharm Res (2015) 32:2384–2409
DOI 10.1007/s11095-015-1631-4

RESEARCH PAPER

In Vitro, *Ex Vivo* and *In Silico* Mechanistic Elucidation of the Performance of an Optimized Porosity-Controlled Multi-Elemental Transbuccal System

Oluwatoyin A. Adeleke • Yahya E. Choonara • Lisa C. du Toit • Pradeep Kumar • Viness Pillay

Received: 4 November 2014 / Accepted: 16 January 2015 / Published online: 29 January 2015

ABSTRACT

Purpose To elucidate the mechanisms of construction and performance of a porosity controlled, multi-elemental transbuccal system employing experimental and computational approaches.

Methods The production of the formulation was guided through a Box-Benkhen design employing homogenization coupled with lyophilization. The physicochemical and physicomechanical properties of the experimental design formulations were quantified with relevant analytical techniques. The influence of changes in porosity measures on the magnitude of these physical properties were explored mathematically. Furthermore, experimental outputs from the Box-Behnken design formulations were fitted into set limits and optimized using the response surface method. The optimized porosity-controlled formulation was subjected to mechanistic experimental and computational elucidations.

Results In general, the changes in magnitudes of studied porosity quantities had significant impact on formulation physicochemical and physicomechanical properties. The generation of an optimized formulation validated the stability and accuracy of the Box-Behnken experimental design. Experimental investigations revealed that the construction of this formulation is as a result of non-destructive physical interactions amongst its make-up compounds while its mechanism of performance is anchored mainly upon a gradual collapse of its ordered porous structure. Furthermore, the molecule mechanics simulations quantitatively predicted the molecular interactions inherent to multicomponent matrix formation and the mucoadhesion mechanism.

Conclusions The fabrication and performance mechanisms of the porosity-controlled transbuccal system was successfully explored.

O. A. Adeleke • Y. E. Choonara • L. C. du Toit • P. Kumar • V. Pillay (✉)
Wits Advanced Drug Delivery Platform Research Unit, Department of Pharmacy and Pharmacology, School of Therapeutics, Faculty of Health Sciences, University of the Witwatersrand, 7 York Road, Parktown 2193 Johannesburg, South Africa
e-mail: viness.pillay@wits.ac.za

KEY WORDS computational modeling · experimental analyses · mechanisms of construction and performance · porosity-controlled · transbuccal system

ABBREVIATIONS

ANOVA	A one-way analysis of variance
CARB 974	Carbopol 974P NF
C-DSC	Cconventional differential scanning calorimetry
CHTS	Chitosan
CP_D	Cumulative drug permeation
DLE	Drug loading efficiency
EMD	Ethanol-based multi-elemental dispersion
ETH 10	Ethylcellulose
EtOH	Ethanol
F_{det}	Peak detachment force
FTIR	Fourier Transform Infrared
GEL	Gelatin
HEC	Hydroxyethylcellulose
J_s	Drug flux
$MDT_{50\%}$	Mean dissolution time for 50% drug release
M_F	Matrix firmness
M_R	Matrix resilience
MS	Magnesium stearate
MTH	Menthol
PBS	Phosphate buffered saline
PCMS	Porosity-controlled multi-elemental system
PS-Na	Phenytoin sodium
PVA	Polyvinyl alcohol
R^2	Correlation coefficient
SEM	Scanning electron microscopy
SP 80	Span 80
T_g	Glass transition

$þ_D$	Average pore diameter
$þ_{SA}$	Cumulative pore surface area
$þ_V$	Cumulative pore volume
T_m	Melting temperature
TM-DSC	Temperature modulated differential scanning calorimetry
W_0	W_1, W_2, W_3, W_4, W_5, Weights of dry mixture before addition of ethanol and water, homogenous blend, cured blend, pre-frozen blend post curing, blend after 24 h lyophilization cycle and completely lyophilized PCMS
WMD	Water-based multi-elemental dispersion
X_{0hr}	Unhydrated PCMS
X_{1h}, X_{2h}, X_{4h}, X_{8h}	Hydrated PCMS at 1, 2, 4 and 8 h respectively
γ	Deformation
ΔC_p	Reversible heat flow due to changes in the magnitude of the heat capacity complex
η	Mean viscosity
λ_{max}	Lambda Max
ω_{adh}	Work of adhesion
ϵ_D	Energy of matrix distortion
κ_p	Permeability coefficient

INTRODUCTION

Porosity-controlled delivery systems have found beneficial drug delivery applications as multi-unit matrices (1,2), biological scaffolds (3–7), xerogels (8), osmotic pumps (9–12), tablets (13,14), nanoparticles (15,16), nanotubes (17) implants (18,19), tissue engineering cements (20), granules (21), pellets (22) and optical devices (23). Solid materials employed as single entities or combinations with either solids or liquids when subjected to physical processes such as grinding, dry or wet mixing, crystallization, lyophilization usually resulted in characteristic cracks or hole structures described as pores (24). A porous structured matrix can be described as a stable, flexible mono- or multi-component system characterized by distinctive aperture/hole structures or void spaces and interconnectors which influence their overall performances (25) while porosity entails the measurement and characterization of void spaces (pore structures) in a materials (26,27). Pores present within a matrix possess the capability to contribute to its exhibited physicochemical and physicomechanical properties and the evaluation of characteristic pore structures of a material can provide salient information about mechanisms of disintegration, dissolution, adsorption and diffusion of drug molecules (24,26,28).

An exponential increase in the applications of porosity-controlled systems for modulating chronological or distributional drug release through viable routes of administration have been observed (25,28,29). They possess outstanding intrinsic characteristics such as stable porous network, high surface area, flexible pore sizes arranged in various distribution patterns, well defined surface properties and their capability to externally and internally interact with biomolecules or cells which make them useful in the construction of any form of delivery system (25,28,30). These unique qualities allow them to adsorb and release drug in a reproducible and predictable manner as well as to load high drug concentrations relative to pore volume, enhance mucoadhesion and augment transmucosal permeation and systemic absorption of biomolecules (25,28). Thus, the configuration and performance of these specialized delivery systems is based on their characteristic porous structure which greatly influences their usefulness and remains an interesting and intellectually challenging subject for systematic exploration (29).

This investigation is centered on delineating the mechanisms of formation and performance of a novel porosity-controlled multi-elemental system (PCMS) fabricated for transbuccal drug delivery utilizing phenytoin sodium (PS-Na) as a model drug. A typical porosity-enabled matrix has been previously employed in loading and controlling the release of PS-Na via the transbuccal route (25). The transbuccal route is easily reachable and well vascularized; allows non-invasive, painless self-administration, controlled absorption of bioactives and the use of retentive dosage forms; has short recovery times after formulation application and an expanse of smooth muscles; easy removal of formulation when required as well as capable to release drug molecules into circulation thereby avoiding pre-systemic metabolism (25,30,31). However, to date, no scientific outputs have reported to elucidate the mechanisms involved in the formation and performance of this unique formulation. Furthermore, porosity-controlled formulations are of great value as they have demonstrated highly valuable biomedical and pharmaco-therapeutic efficacy as mentioned earlier. Consequently, a closer look into their underlying mechanisms explored in this investigation may provide valuable information for improving and/or expanding their medical applicability. The PCMS under study was fabricated and optimized using multiple polymeric and non-polymeric molecules by homogenization and lyophilization guided through a high performance Box-Behnken experimental design. The impact of porosity parameters on the magnitude of salient physical and mechanical textural properties was evaluated mathematically whereas the mechanisms of construction and performance were elucidated utilizing experimental and computational modeling approaches.

MATERIALS AND METHODS

Materials

Phenytoin sodium (PS-Na), potassium dihydrogenphosphate monobasic buffer salt, phosphoric acid (85%), methanol (HPLC grade), gelatin (GEL), polyvinyl alcohol (PVA) (molecular weight = 72,000), magnesium stearate (MS) were purchased from Sigma Chemical Company (St. Louis, USA). Chitosan (CHTS) (medium molecular weight, 75–85% deacetylated) and menthol (MTH) were obtained from Warren Chem Specialties, Johannesburg, South Africa. Hydroxyethylcellulose (HHX 250 Pharm) (HEC) was purchased from Hercules, Aqualon (Germany). Span 80 (SP 80) and 95% ethanol (EtOH) were procured from Merck Chemicals (Darmstadt, Germany) and Saarchem (Johannesburg, Gauteng, South Africa) respectively. Carbopol 974P NF (CARB 974) and Ethylcellulose (Ethocel® 10) (ETH 10) were acquired from Noveon, Inc, (Cleveland, Ohio, USA) and Protea Industrial Chemicals (Pty) Ltd (Wadesville, South Africa) respectively. All other reagents utilized were of analytical grade and used as received.

Fabrication of the PCMS Guided Through a Box-Behnken Statistical Design

Variant PCMS formulations were fabricated utilizing interphase, co-particulate, co-solvent, homogenization, prefreezing and lyophilization (25) employing 15 combinations of independent variables generated using a 2-level, 3 factor and 3 centre points Box-Behnken quadratic design (Minitab Statistical Software, Version 16, Minitab Inc., State College, PA, USA). Three categories of independent variables highlighted below were employed in fabricating the PCMS:

(i) The water-based multi-elemental dispersion (WMD) composed of PVA, HEC, CARB 974, GEL and DW
(ii) The ethanol-based multi-elemental dispersion (EMD) made up of ETH 10, MS, MTH, CHTS and EtOH and
(iii) SP 80.

Tables I and II present the 2 levels of the independent variables employed and the experimental design template for the 15 experimental runs respectively. The lower and upper limits for the factors were set based on their ability to form stable PS-Na loaded PCMS using minimal quantities of each component.

Combinations of solutes according to specifications in Table II were separately dispersed in water and ethanol to form the WMD and EMD respectively. Each batch of formulation produced an average of 25 PCMSs and each contained 50 mg PS-Na which was dispersed in the WMD. Specific quantities of SP 80 were first mixed with WMD and then the mixture with the EMD (Table II) to form a stable, continuous-phased blend. Overall, the formation of the homogenous multi-elemental blend was aided with a laboratory scale homogenizer (Polytron® 2000, Kinematica AG, Switzerland) for 10 min and cured in the dark for 30 min. Each PCMSs was produced by pipetting 1 mL of the blend into specialized, pre-oiled (using liquid paraffin) polystyrene moulds (10 mm × 10 mm), pre-freezing at −72°C for 24 h and lyophilizing using a freeze dryer (Bench Top 2 K, Virtis, New York, USA) set at −55 ± 2°C and 0.42 mBar for 48 h. After lyophilization, fabricated PCMSs were weighed on a

Table I Independent Variables Employed in the Box-Behnken Design Template

Independent Variables	Levels		Units
	Low	High	
WMD	0	2	mg/20, 25,30 mL of water
EMD	3	5	mg/13, 11,7 mL of ethanol
SP 80	0.3	0.7	mL

Table II Box-Behnken Template for the Preparation of the PCMS Formulations

Formulation	Composition		
	WMD (mg/20, 25,30 mL)	EMD (mg/13, 11,7 mL)	SP 80 (mL)
1	0	5	0.5
2	0	3	0.5
3*	1	4	0.5
4	0	4	0.7
5*	1	4	0.5
6	1	3	0.3
7	1	5	0.7
8	2	3	0.5
9	1	5	0.7
10	2	4	0.3
11*	1	4	0.5
12	2	5	0.5
13	2	4	0.7
14	1	5	0.3
15	0	4	0.3

WMD: 0 - PVA (800 mg) + HEC (350 mg) + GEL (400 mg) + CARB (100 mg) + DW (30 mL); 1 - PVA (550 mg) + HEC (525 mg) + GEL (350 mg) + CARB (150 mg) + DW (25 mL); 2 - PVA (300 mg) + HEC (700 mg) + GEL (300 mg) + CARB (200 mg) + DW (20 mL). EMD: 3 - CHTS (550 mg) + MS (350 mg) + MTH (200 mg) + ETH 10 (400 mg) + EtOH (13 mL); 4 - CHTS (425 mg) + MS (325 mg) + MTH (250 mg) + ETH 10 (500 mg) + EtOH (10 mL); 5 - CHTS (300 mg) + MS (300 mg) + MTH (300 mg) + ETH 10 (600 mg) + EtOH (7 mL)

* Centre points

laboratory scale balance (Mettler Toledo, AB104-S, Microsep Pty Ltd, Switzerland) and stored under controlled humidity in closed glass jars for further testing.

Measurement of Salient Physicochemical and Physicomechanical Parameters of the 15 Experimental Design PCMS Formulations

Evaluation of In Vitro Drug Release Performance of the PCMS Variants

Drug release was evaluated in triplicate by submerging every formulation into 25 mL simulated saliva with a pH of 6.8 (32) contained in a closed 50 mL capacity glass jars at 37 ± 0.5°C and 20 rpm in a shaking incubator (Orbital Shaker Incubator, LM-530, Lasec Scientific Equipment, Johannesburg, South Africa). 3 mL samples were manually withdrawn from the dissolution medium at specific time intervals over 8 h (30, 60, 120, 240, 360, and 480 min) and filtered through a 0.45 μm pore size Cameo Acetate membrane filter (Millipore Corporation, Bedford, MA, USA). The sink conditions were maintained by replacing withdrawn volume with freshly prepared simulated saliva at each sampling time. The amount of PS-Na released was determined utilizing the Ultraviolet Spectrophotometer (Cecil CE 3021, 3000 Series, Cecil Instruments, Cambridge, England) at λ_{max} = 206 nm. In some instances, drug release evaluation outputs were computed as mean dissolution time ($MDT_{50\%}$) which is determined as the sum of the individual periods of time during which a specific fraction of the total drug dose (50% was selected in this case) is released (33,34) (Eq. 1).

$$MDT_x\% = \sum_{i=1}^{n} t_i \frac{M_t}{M_\infty} \tag{1}$$

Where M_t is the fraction of dose released in time t_i, $t_i = (t_i + t_{i-1})/2$ and M_∞ corresponds to the loading dose.

Determination of Drug-Loading Efficiency

Drug loading efficiency (DLE) of each PCMS was computed in triplicate utilizing Eq. 2.

$$\%DLE = \frac{A_d}{T_d} \times 100 \tag{2}$$

Where DLE = drug loading efficiency (% w/w), A_d = actual amount of drug loaded (mg) and T_d = theoretical amount of drug loaded (mg).

For each assay, 100 mL of simulated saliva was used to completely dissolve each PCMS with the aid of the Polytron® 2000 laboratory homogenizer (Kinematica AG, Switzerland). Afterwards, 2 mL sample was manually collected, appropriately diluted, filtered through a 0.45 μm pore size Cameo Acetate membrane filter (Millipore Corporation, Bedford, MA, USA) and analyzed utilizing the Ultraviolet Spectrophotometer (Cecil CE 3021, 3000 Series, Cecil Instruments, Cambridge, England) at 206 nm. Generated absorbance values (y) were fitted into the linear polynomial equation ($y = 16.516x$; $R^2 = 0.995$) of the PS-Na calibration curve to generate A_d which was substituted into Eq. 2 to give the %DLE values.

Assessment of Ex Vivo Drug Permeation Properties With Porcine Buccal Mucosa

Fresh porcine buccal mucosa was harvested from the cheek region of slaughtered domestic large white pigs from a regional abattoir (Mintko Meat Packers, Krugersdorp, Johannesburg, South Africa). Excess surrounding tissues were surgically dissected from the harvested buccal mucosal specimens to an average thickness was 0.9 ± 0.1 mm measured using a manually operated vernier caliper (25 × 0.01 mm capacity). Subsequently, ready mucosal specimens were snap frozen in liquid nitrogen and stored at −70°C for up to 2 months as reported in previous research outputs (35,36) until analysis. With each permeation experiment, frozen mucosal specimens were thawed and re-hydrated to regain elasticity by immersing them in 100 mL phosphate buffered saline (PBS, pH 7.4) at 37 ± 0.5°C for 20 min. After re-hydration, mucosal disks (diameter = 1.5 ± 0.1 cm and surface area = 2.27 ± 0.81 cm^2) were surgically dissected from the harvested specimen and immediately carefully mounted onto the flow through Franz type diffusion cells (Membrane transport systems, V3, Permegear, Amie Systems, USA) connected to a water bath with a circulating heating system (CPE 100, Labcon, Maraisburg, Gauteng, South Africa) set at 37 ± 0.5°C. The receiver compartment contained 10 mL simulated plasma of pH 7.4 (36) while the donor compartment contained a 2 mL solution of the PCMS in simulated saliva. The content of the receiver was continuously magnetically stirred to achieve uniform mixing and samples were collected at preset time intervals over 30, 60, 120, 240, 360, 480 min. 2 mL sample was withdrawn from the receiver compartment and replaced with the same volume of fresh simulated plasma. Withdrawn samples were spectrophotometrically assayed for PS-Na at 206 nm and the cumulative drug permeation (CP_D) was calculated. All assays were carried out in triplicate.

In addition, drug flux (J_s) through the membrane was calculated at the steady state per unit area by linear regression analysis of permeation data following Eq. 3 while the permeability coefficient (κ_p) was computed using Eq. 4 (36,37).

$$J_s = \frac{Q_r}{A \times t} \tag{3}$$

Where J_s is the drug flux (mg cm^{-2} min^{-1}), Q_r is the quantity of PS-Na that diffused through the porcine buccal mucosa into the receptor compartment (mg), A is the active cross-sectional area accessible for diffusion (cm^2) and t is the time of exposure in minutes.

$$\kappa_p = \frac{J_s}{C_d} \tag{4}$$

Where J_s is the flux calculated at steady state (Eq. 3), C_d is the drug concentration in the donor compartment (mg cm^{-3}).

Measurement of Ex Vivo Mucoadhesivity Using Porcine Buccal Mucosa as a Model

The *ex vivo* mucoadhesive strength of the PCMS was evaluated in triplicate using a calibrated Texture Analyzer (TA.*XTplus*, Stablemicro Systems, Surrey, England) fitted with a 10 mm diameter cylindrical stainless steel probe. Freshly isolated porcine buccal mucosa (diameter = 1.5 ± 0.1 cm and surface area = 2.27 ± 0.81 cm^2) was affixed unto the cylindrical probe whilst the PCMS was placed on the stage of the machine. Both surfaces were well aligned to ensure that they came into contact during measurements. Measurement settings were: contact force (0.1 g), pre-test speed (2 mm/s), test speed (0.5 mm/s), post-test speed (10 mm/s), applied force (1 N), return distance (8 mm), contact time (10 s), trigger type (auto) and trigger force (0.049 N). For each PCMS variant assessed, the surface of the mucosa was hydrated uniformly by soaking it in 2 mL simulated saliva placed in a glass petri dish for 5 min. Thereafter, the mucosa was lowered towards the stage to make contact with the PCMS. Mucoadhesive capacity quantified as peak detachment force (F_{det}) and work of adhesion (ω_{adh}) were calculated from the generated force-distance graphical outputs as the maximum force needed to separate the PCMS from the tissue and the area under the force-distance curve, respectively.

Quantitative Determination of Porosimetric Parameters

The average pore diameter ($þ_D$), cumulative pore volume ($þ_V$) and cumulative pore surface area ($þ_{SA}$) were quantified in triplicate using the surface area and porosity analyzer equipped with the ASAP 2020 V3.01 software (Micromeritics, ASAP 2020, Norcross, GA, USA). The Barrett, Joyner and Halenda (BJH) method which is based on the Kelvin equation (Eq. 5) was employed for these computations (24).

$$\ln\frac{P}{P_0} = \frac{2\gamma\gamma\cos\theta}{RTr_m} \tag{5}$$

Where P = the critical condensation pressure, γ = liquid surface tension, v = molar volume of the condensed adsorptive, θ = contact angle between the solid and condensed phase (taken to be zero when adsorptive gas is nitrogen, hence cos θ = 1), r_m = mean radius of curvature of the liquid meniscus, P/P_0 = relative pressure, R = universal gas constant and T = absolute temperature.

This investigation was conducted in the degassing and analysis stages using a dry sample weight of 130 ± 10 mg for all 15 formulations. Samples were degassed to remove air, gases and other adsorbed atmospheric vapor and species from the sample surface. The operating settings were temperature ramp rate (10°C/min), target temperature (30°C), evacuation rate (50 mmHg/s), unrestricted evacuation (30 mmHg), vacuum set point (500 μmHg), evacuation time (60 min), heating hold temperature (35°C), hold time (900 min), evacuation and heating hold pressure (100 mmHg) and analysis time (400 min).

Rheological Investigations of the Homogenous Blends

The rheological characteristics in terms of mean viscosity (η) and deformation (γ) of the un-lyophilized homogenous blends used in preparing the PCMS and their overall influence on the matrix integrity were investigated in triplicate utilizing a Modular Advanced Rheometer System equipped with the Haake Rheowin software (ThermoHaake MARS, Thermo Fischer Scientific, Karlsuhe, Germany). The rheometer stage was filled with 1 mL of homogenous blend for each formulation. The rotor C35/1° Titan sensor type was employed and measurement was conducted at an operational temperature of 25°C, analytical contact time of 180 s, controlled rate ranging from 0 to 5 s^{-1} and constant shear rate of 0 to 500 s^{-1}. Mean viscosity (η) and deformation (γ) values were computed at an average, constant shear rate of 250 s^{-1}.

Measurement of the Physicomechanical Strength of the PCMS Variants

The physicomechanical characteristics of the PCMS variants were quantified as matrix resilience (M_R), energy of matrix distortion ($Є_D$) and matrix firmness (M_F). These parameters were chosen for this evaluation because they have been reported to noticeably influence formulation integrity, extent of polymeric chain entanglement and disentanglement as well as drug release trends (25,38). A calibrated TA.*XTplus* Texture Analyzer (load cell = 5 kg trigger and force = 0.5 N) fitted with a cylindrical steel probe (50 mm diameter) was employed for the determination of M_R (compression strain = 50%) while the $Є_D$ and M_F (compression force = 40 N) were measured using a flat-tipped steel probe (2 mm diameter). All measurements were performed in triplicate at a pre-test, test and post-test speed of 1 mm/s, 0.5 mm/s and 10 mm/s

respectively. ϵ_D (J) and M_F (N/mm) were computed employing generated force-distance profile as the area under the curve (AUC) and gradient between the initial and maximum force attained respectively. On the other hand, M_R (%) was calculated as a ratio between the two AUCs from the force-time graph.

Evaluation of the Impact of Porosity Regulation on Relevant Physical Quantities Using a Mathematical Approach

The influences of porosity parametrical changes on the magnitude of specific quantifiable physical properties which are paramount to the performance of the PCMS were evaluated. In this regard, β_D and β_{SA} were selected as measures of porosity and the physical quantities selected were $MDT_{50\%}$, DLE, F_{det} and CP_D, η and M_R. A polynomial mathematical expression was employed to visualize the existing relationships by assessing the linearity/non-linearity of graphical outputs which were validated with the correlation coefficient, R^2. The Sigma Plot, Version 11 software (Systat Software Inc. California, USA) was employed for this purpose.

Optimization of Experimental Design PCMS Formulations

Experimental outputs from the Box-Behnken template were fitted within set limits for predicting the optimal PCMS formulation. Optimization was simultaneously approached using a Response Surface Optimizer (Minitab software, Version 16, USA) to set constraints to obtain levels of independent variables that will concurrently manipulate relevant response parameters to yield the desired statistically optimal levels. On this basis, a target level was set for the $MDT_{50\%}$ while the DLE, F_{det} and CP_D were maximized with respect to the expected optimal behaviour. A desirability function of 0.96 which is indicative of the accuracy and efficiency of the statistical optimizer was obtained. A one-way analysis of variance (ANOVA) was applied to estimate the significance and reliability of the statistical model. The model-dependent terms employed in this study included *p-values* set at 95% confidence level ($p \leq 0.05$) and correlation coefficient ($R^2 > 0.90$) (Table III).

An Experimental Approach to Elucidating the Mechanisms of Configuration and Function of the Optimized PCMS

Assessment of Possible Structural Transitions During PCMS Preparation

The Fourier Transform Infrared (FTIR) spectra for the un-lyophilized optimized homogenous blend and lyophilized PCMS were recorded on the Perkin Elmer 100 Series FTIR Spectrophotometer (Beaconsfield, UK) equipped with the Spectrum V 6.2.0 software. 10 mg sample was placed on the sample holder situated on the machine stage. The instrument stage was cleaned with methanol before each sample (10 mg) was placed upon it for analysis. Blank background scans were taken before sample analysis which was performed at wavenumbers ranging from 4000 to 600 cm^{-1}, scan time = 32 scans and resolution of 4 cm^{-1}. All recorded output scans were computed as an average of five repeated scans.

Determination of Thermal Behavior Using Differential Scanning Calorimetry

The thermal properties of the optimized un-lyophilized blend, lyophilized PCMS and each additive employed in its fabrication were analyzed using the conventional differential scanning calorimetry (C-DSC). Thereafter, temperature modulated differential scanning calorimetry (TM-DSC) was applied to the un-lyophilized blend and lyophilized PCMS to visualize important hidden transitions. All DSC curves were recorded on a DSC1, STAR^e System equipped with computational software for analysis (Mettler Toledo, Switzerland). Respective samples (5 mg) were placed in crimped aluminium pans. For the C-DSC determinations, the un-lyophilized blend was heated within the range of −35 to 500°C while the constituting compounds and lyophilized PCMS were heated from −35 to 350°C at a rate of 10°C/min under inert nitrogen as a purging gas. TM-DSC measurements were conducted using heating rate of 1°C/min for a period of 60 s, modulation amplitude of 0.8°C, loop increment and segment of 0.8 and 1 respectively and an automatically computed count of 212 over a selected temperature ranges. The

Table III Numerical Values and Levels of Statistical Significance of the Response Parameters Employing ANOVA

Parameters	Statistical goal	Lower limit	Upper limit	*p-values*	R^2	Optimization goal
$MDT_{50\%}$ (minutes)	Target	80.000	100.000	0.031	0.907	90.000
DLE (%)	Maximum	90.000	100.000	0.013	0.948	100.000
F_{det} (N)	Maximum	1.100	1.200	0.048	0.905	1.200
CP_D (%)	Maximum	80.000	90.000	0.011	0.991	90.000

curves generated were smoothed at an order of 1 to 200 points and all experiments were carried out in triplicate. The temperature ranges employed for the respective samples are: un-lyophilized homogenous blend: −35–55°C, 60–140°C, 145–300°C and 305–450°C; lyophilized PCMS: 0–120°C, 150–260°C. These temperature ranges were selected as these were the segments within which salient thermal activities had occurred.

Evaluation of Changes in Sample Weight Before and After Lyophilization

Samples were weighed at different phases in the preparation of the PCMS. This included dry mixture before addition of ethanol and water for homogenization (W_0), homogenous blend (W_1), cured blend (W_2), pre-frozen blend post curing (W_3), blend after 24 h lyophilization cycle (W_4) and completely lyophilized PCMS (W_5). All measurements were done in triplicate employing a laboratory weighing balance (Mettler Toledo, AB104-S, Microsep Pty Ltd, Switzerland).

Evaluation of Changes in Physicomechanical Texture

Textural analysis was used to quantify the variations in physicomechanical strength of measurable samples which were a mixture of the unhydrated ingredients, WMD, EMD, un-lyophilized homogenous blend before and after curing and the lyophilized PCMS. The values obtained from these samples were compared to dry mixture of the constituting compounds. For easy and relatively accurate measurement, this dry mixture was placed in a plastic tub and subjected to physicomechanical testing. The parameters measured were M_F and ϵ_D. Other experimental stipulations undertaken were the same as those described earlier within the manuscript.

Mechanism of Performance

In an attempt to visualize and elucidate the possible mechanisms guiding the action of the PSCM, formulations were separately placed into 25 mL of simulated saliva contained in closed 100 mL capacity glass jars maintained at 37 ± 0.5°C and 20 rpm in a shaking incubator (Orbital Shaker Incubator, LM-530, Lasec Scientific Equipment, Johannesburg, South Africa). At specified time intervals (1, 2, 4, 8 h), remnants of dissolved PCMS were removed, dried at 35 ± 0.5°C (Memmert 854, Schwabach, Western Germany) to a constant weight, analysed and compared with the unhydrated PCMS formulation. Each tested sample were represented as X_{0h} – unhydrated PCMS, X_{1h} – hydrated PCMS at 1 h, X_{2h} – hydrated PCMS at 2 h, X_{4h} – hydrated PCMS at 4 h and X_{8h} – hydrated PCMS at 8 h. These samples were analysed in triplicate employing the following techniques:

Infrared Spectrophotometry

About 10 mg sample (X_{0h} X_{1h} X_{2h} X_{4h} X_{8h}) size was analysed with the Perkin Elmer FTIR Spectrophotometer following the procedure described earlier.

Scanning Electron Microscopy

The changes in the porous surface architecture of both hydrated and unhydrated PCMS samples (X_{0h} X_{1h} X_{2h} X_{4h} X_{8h}) were viewed and characterized employing scanning electron microscopy (SEM). Samples (2 mm diameter × 2 mm thickness) were sputter-coated with gold-palladium and viewed six times from different angles under a JSM-840 Scanning Electron Microscope (JEOL 840, Tokyo, Japan) at a voltage of 20 keV and a magnification of 1000×.

Gravimetric Analysis

In vitro matrix erosion patterns were assessed by separately weighing (Mettler Toledo, AB104-S, Microsep Pty Ltd, Switzerland) each experimental sample (X_{0h} X_{1h} X_{2h} X_{4h} X_{8h}). All determinations were done in triplicate and Eq. 6 was employed to determine the fractional mass loss in $^{w}/_{w}$.

$$\text{Fractional Mass Loss} = \frac{\text{Original Mass} - \text{Residual (dry) Mass}}{\text{Original Mass}} \tag{6}$$

Analysis of Changes in Physicomechanical Texture

Changes in matrix physicomechanical textural strength were measured in terms of matrix firmness (M_F) and energy of matrix distortion (ϵ_D) using textural profiling analysis. The methodology for measuring physicomechanical strength mentioned earlier was utilized.

Prediction of the underlying mechanisms of configuration and performance of the PCMS by computational modeling

The overall performance of the PCMS formulation is dependent on complex mechanisms of configuration and performance of its three-dimensional porous structure. Consequently, chemometric and structural computational modeling methods were employed to evaluate and predict these underlying mechanisms as well as substantiate the experimental outputs. In addition, semi-empirical quantum mechanics were employed to generate molecular interactions and computational energy paradigms of the PCMS components based on inherent interfacial homogenization and lyophilization phenomena underlying the mechanisms of configuration and performance as provided by the multi-elemental blend and

solid state PCMS. Models and graphics supported on the stepwise mechanistic molecular transitions were generated in our laboratory using the ACD/I-Lab, V5.11 (Add-on) software (Advanced Chemistry Development Inc., Toronto, Canada, 2000).

All modeling procedures and computations, including energy minimizations in Molecular Mechanics, were performed using HyperChem™ 8.0.8 Molecular Modeling Software (Hypercube Inc., Gainesville, FL, USA) and ChemBio3D Ultra 11.0 (CambridgeSoft Corporation, Cambridge, UK). The 3D structures of polyvinyl alcohol (PVA) and Carbopol 974P NF (polyacrylic acid; PAA) were archetyped using ChemBio3D Ultra in their syndiotactic stereochemistry as 3D models, whereas the structures of ethylcellulose (EC), Hydroxyethylcellulose (HEC) and chitosan (CHT) were built from standard bond lengths and angles using the Sugar Builder Module on HyperChem 8.0.8. The structures gelatin (GEL; Glycine-Proline-Hydroxyroline) and glycosylated mucopeptide analogue (MUC) mucin was generated using the sequence editor module on HyperChem 8.0.8. The glycosylation was performed at the threonine amino acid residues. The models were primarily energy-minimized using the MM+ Force Field algorithm and the resulting structures were once again energy-minimized using the AMBER 3 (Assisted Model Building and Energy Refinements) Force Field algorithm. The conformer having the lowest energy was used to develop the polymer-polymer and polymer-mucin complexes. A complex of one polymer molecule with another was assembled by parallel disposition and the energy-minimization was repeated to generate the final models: EMD (CHT-EC), WMD (PAA-PVA-HEC-GEL), EMD-WMD, and EMD-WMD/MUC. Full geometrical optimization was conducted in vacuum employing the Polak–Ribiere Conjugate Gradient method until an RMS gradient of 0.001 kcal/mol was reached [39].

RESULTS AND DISCUSSION

Quantification of Relevant Physicochemical and Physicomechanical Properties of the Experimental Design PCMS Formulations

Overall the 15 formulations were hemispherical in geometry with weights ranging between 133.95 mg and 178.75 mg (Table IV) with a diameter and breadth of 8 mm and 4 mm respectively. Each experimental design PCMS formulation exhibited diverse drug release behaviours attributable to the differences in their composition, variations in porous structures, degrees of homogenization and lyophilization. Drug release behaviour was quantified employing the $MDT_{50\%}$ values (Eq. 1, Table IV) which were categorized as low ($MDT_{50\%} < 110.00$ min) and high ($MDT_{50\%} > 110.00$ min) which represented rapid and prolonged drug release trends respectively for these formulations. The quantity of co-particles contained in each formulation had considerable multifaceted effects on the drug release pattern. Generally, formulations that comprised of higher levels of hydrophobic solutes than the hydrophilic components displayed more controlled release patterns ($MDT_{50\%} > 110.00$ min) while those with higher concentration of the hydrophilic components relative to the hydrophobic solutes showed less controlled drug release behaviours ($MDT_{50\%} < 110.00$ min). Also, the volume ratio of the pore formers, DW and EtOH, can be included as one of the factors which impacted the differences in the $MDT_{50\%}$ values because of the differences in their boiling points (EtOH = 78.30°C and DW = 100.00°C) and densities (EtOH = 0.70 g/mL and DW = 1.00 g/mL) which can influence the processes of pre-freezing and sublimation. Therefore, EtOH with lower boiling point and density can solidify and sublime quicker than DW thereby allowing the formation of a more open porous structure while DW on the other hand can congeal and sublime at slower rate resulting in the formation of closer knitted porous configuration.

On the whole, the differences in the pore-forming capacities of DW and EtOH can influence processes of matrix hydration and drug release for each formulation. Effective drug loading ranging between 53.14% and 99.10% was achieved. No particularly unique trend was noticed amongst the formulations but the concentration of PVA appeared to distinctly impact drug loading capacities as formulation 4 (800 mg PVA) displayed a higher DLE value (99.10%) than formulation 13 (300 mg PVA) with DLE of 53.14%. Obtained%DLE values are presented in Table IV. The PCMSs initiated and sustained the permeation of the PS-Na molecules through the porcine buccal mucosa at different levels as indicated by the values of the CP_D, J_s and κ_p (Table IV). The different concentrations of permeation enhancers (SP 80, CHTS, MTH) employed in the fabrication of the PCMS displayed extensive synergistic and efficient permeation effects at mid to low factor levels (Table I and II) while at higher factor levels (Tables I and II), permeation impacts were lower based on measured CP_D values (Table IV). Js, a measure of rate of drug penetration over the mucosa surface area, differed for the formulations. In other word, drug flux determines that quantity of drug molecules that permeated through the sample tissue. κ_p, a measure of the distance traveled by the drug molecules per minute also varied slightly for each formulation (Table IV). The minimal differences observed with the values obtained for each formulation can indicate that the tissue permeation velocity is dependent on the concentration of drug contained in the donor compartment, the composition of each PCMS as well as the drug flux. The measures of matrix porosity, $þ_D$, $þ_V$ and $þ_{SA}$, yielded values of 40–100 Å, 6.5×10^{-4}–5×10^{-3} cm^3/g and 28–800 cm^2/g respectively (Tables IV and V).

Table IV Values of Measured Physicochemical and Physicomechanical Parameters for the Experimental Design PCMS Formulations

PCMS	Weight (mg)	$MDT_{50\%}$ (min)	DLE (%)	CPD (%)	Js ($mgcm^{-2}$ min^{-1}) $\times 10^{-4}$	κ_p ($mgcm^{-3}$) $\times 10^{-4}$	$þ_D$ (Å)	$þ_{SA}$ (cm^2/g)
1	124.701	104.000	58.601	65.633	34.451	12.051	44.141	28.380
2	128.351	85.000	80.544	78.271	48.940	14.922	71.566	245.740
3	128.754	98.000	95.142	74.871	50.571	14.291	92.407	395.150
4	121.953	105.000	99.100	39.065	26.950	7.170	45.279	714.654
5	130.004	104.500	94.647	75.192	60.310	13.801	85.123	445.475
6	126.203	220.000	99.023	44.941	40.841	8.254	79.462	213.330
7	133.754	225.000	97.543	25.021	24.640	4.590	67.778	315.540
8	129.102	88.500	66.830	70.463	36.571	12.932	62.777	396.595
9	123.254	15.000	83.270	64.933	38.991	11.921	64.694	346.470
10	129.703	185.000	79.282	26.711	16.452	4.902	74.419	244.680
11	127.252	100.000	94.851	79.440	58.491	14.584	89.822	421.795
12	132.854	210.000	98.643	55.470	39.453	10.181	70.784	236.605
13	126.755	90.000	53.140	62.513	25.790	11.471	73.814	220.150
14	132.408	161.000	81.380	76.020	57.161	14.691	48.402	590.485
15	131.607	22.500	79.181	82.211	40.751	16.381	50.413	758.245

Standard deviations (SD): Weight; SD ≤ 1.8000 mg, $MDT_{50\%}$; SD ≤ 5.0800 min, DLE; SD ≤ 3.7700%, CPD; SD ≤ 1.4100%, Js; SD ≤ 1.9900×10^{-4} $mgcm^{-2}$ min^{-1}, κ_p; SD ≤ 1.020×10^{-4} $cmmin^{-1}$, $þ_D$; SD ≤ 5.000 Å, $þ_{SA}$; SD ≤ 20.970 cm2/g in all cases (N = 3)

These numerical measures show that the overall performance of the PCMSs is subject to their pore structure, diameter and distribution which also signify the integrity and configuration of the interconnectors as well as the surface area of the porous formulation.

Based on the values of $þ_D$, all 15 PCMS formulation can be described as mesoporous in nature (24). The PCMSs demonstrated quantifiable capabilities to adhere to a typical buccal mucosal tissue based on the varying magnitudes of F_{det} (0.964–1.042 N) and ω_{adh} (0.0014–0.0028 J) (Table V). No specific mucoadhesive trend was observed indicating that the mucoadhesive agents, gelatin and carbopol 974 employed during formulation preparation reinforced each other in influencing the overall mucoadhesive potency which explains

Tables V Values of Measured Physicochemical and Physicomechanical Parameters for the Experimental Design PCMS Formulations

PCMS	$þ_V$ (cm^3/g)	F_{det} (N)	ω_{adh} (J) $\times 10^{-3}$	η(Pa.s) × 104	$\gamma \times 10^4$	MR (%)	ϵ_D (J)	MF (N/mm)
1	0.001	0.964	1.673	7.893	1.488	2.975	0.052	4.430
2	0.004	1.011	2.821	86.580	1.514	2.230	0.033	5.214
3	0.007	1.010	2.363	52.710	1.509	2.080	0.014	5.449
4	0.008	1.020	1.873	8.540	1.487	2.221	0.049	5.168
5	0.007	1.014	1.765	51.990	1.514	2.065	0.018	5.518
6	0.004	1.025	1.634	14.840	1.516	2.195	0.053	4.991
7	0.005	1.022	1.489	22.600	1.492	2.288	0.058	4.904
8	0.006	1.012	2.807	12.570	1.499	2.101	0.034	4.671
9	0.006	1.023	1.833	10.120	1.501	1.590	0.052	3.404
10	0.005	1.042	2.202	35.170	1.502	2.067	0.034	4.889
11	0.007	1.013	1.836	54.810	1.507	2.069	0.015	5.550
12	0.004	1.008	1.743	11.850	1.508	2.142	0.042	5.006
13	0.005	1.014	2.022	26.760	1.488	2.253	0.035	4.824
14	0.007	1.023	1.436	55.080	1.488	1.024	0.046	4.082
15	0.010	1.013	2.224	51.150	1.510	1.922	0.023	4.998

Standard deviations (SD) : F_{det}; SD ≤ 0.025 N, ω_{adh}; SD ≤ 2.830×10^{-4} J, η; SD ≤ 0.002 × 104 Pa.s, γ; SD ≤ 0.041, MR; SD ≤ 0.407%, ϵ_D; SD ≤ 0.015 J, MF; SD ≤ 0.566 N, $þ_V$; SD ≤ 7.7400×10^{-4} cm^3/g in all cases (N = 3)

why all 15 formulations demonstrated a level of mucoadhesive competencies. With reference to this investigation, viscosity can be described as quantifying the resistance of the respective homogenous blend to flow with the application of an external compressive force. Generally, the behaviour of these blends was non-Newtonian because their viscosities were dependent upon shear conditions. Computed η values differed amongst formulations but ranged from 0.7893×10^4 to 8.6580×10^4 Pa.s) (Table V). Relating the variations in values of viscosity to measures of porosity per formulation as described earlier, it can be inferred that the degree of blend viscosity has an effect on the process of pre-freezing and sublimation during lyophilization which eventually impacts the nature of the final porous structure. Rheological deformation (γ) on the other hand describes magnitude of change in internal structure of the homogenous blend due to an applied compressive external force and this was relatively consistent for all 15 blends (1.4880×10^4 and 1.5140×10^4) (Table V). This outcome signifies that the blends are robust and stable which can indicate the absence of irreversible, destructive chemical interactions amongst chemical components during formulation fabrication. The physicomechanical parameters M_R, ϵ_D and M_F (Table V), are measures of matrix integrity and strength. Specific to this set of formulations, a direct relationship was observed to exist between the values of M_R and M_F while ϵ_D showed an indirect correlation. It was noticed that the presence of higher levels of PVA, MS and ETH 10 (matrix stiffeners) produced formulations with elevated M_R and M_F and reduced ϵ_D relative to others containing lower levels of the matrix stiffeners. The enlisted numerical magnitudes of these parameters suggest that the PCMSs have relatively low elasticity and resistance to mechanical strain which may be associated with their porous nature.

Construction and Testing of the Optimized PCMS

An optimized PCMS formulation that weighed 175.49 ± 3.98 mg was developed based on the statistical procedure described earlier (Table VI). Statistical analysis further confirmed the impact of formulation variables on measured response parameters ($MDT_{50\%}$, DLE, F_{det} and CP_D). Experimental and statistically fitted outputs were well correlated depicting the suitability and stability of the quadratic design (Table VII).

Table VI Levels of Formulation Variables Utilized for the Fabrication of the Optimized PCMS

Composition	Optimized Level
WMD	0.00 mg/30 mL of water
EMD	4.50 mg/9 mL of ethanol
SP 80	0.50 mL

WMD: 0 - PVA (800 mg) + HEC (350 mg) + GEL (400 mg) + CARB974 (100 mg) + DW (30 mL); EMD: 4.5 - CHTS (362.5 mg) + MS (312.5 mg) + MTH (275 mg) + ETH 10 (550 mg) + EtOH (9 mL)

Determination of the Relationship Between the Porosimetric Parameters and Measured Physical Quantities Using the Experimental Design PCMS Formulations

Generally, the direct and indirect mathematical linear fitting approach employed revealed the nature of relationship between selected measures of porosity ($þ_D$ and $þ_{SA}$) and the selected physicochemical and physicomechanical parameters. Figures 2(a–f) and 3(a–f) illustrate the graphical representations of the outcomes of this set of computations while the correlation coefficient (R^2) values specified the type of relationship which exists between each set of compared parameter. In this regard, $R^2<0.5$ indicate an indirect/inverse correlation while $R^2>0.5$ signify a direct/dependent relationship. Overall, $þ_D$ and $þ_{SA}$ influenced the magnitude of the investigated response parameters either directly or indirectly. A direct relationship was observed between $þ_D$ and $MDT_{50\%}$ ($R^2=0.861$), CP_D ($R^2=0.915$), F_{det} ($R^2=0.605$),%DLE ($R^2=0.922$) and η ($R^2=0.827$) while a reverse trend was observed with M_R ($R^2=-0.692$) (Fig. 1). This indicates that with the PCMS formulations having relatively larger pore sizes enhances transbuccal permeation of drug molecules, mucoadhesion and drug loading while a more viscous homogenous blend employed in their preparation produces formulations with appropriately larger pores. With drug release, it is observed that an increase in $þ_D$ results in an increase in the mean dissolution time which is indicative of prolonged drug release. This shows that the pores present within the PCMS possess unique capabilities of modulating the release of PS-Na molecules. An increase or decrease in $þ_D$ was noticed to reduce or elevate the magnitude of M_R respectively. This behaviour can be associated with the presence of more or less air pockets within the system resulting in a reduction or increase in internal elasticity on the application of an external force.

The $þ_{SA}$ had a direct relationship with the CP_D ($R^2=0.716$) and F_{det} ($R^2=0.699$) while an inverse association was observed with $MDT_{50\%}$ ($R^2=-0.511$),%DLE ($R^2=-0.541$),

Table VII Comparison of the Fitted and Experimental Values of the Response Parameters

Response parameters	Fitted response	Experimental response
$MDT_{50\%}$ (minutes)	90.00	94.10 ± 2.90
DLE (%)	100.00	99.72 ± 3.56
F_{det} (N)	1.20	1.18 ± 0.05
CP_D (%)	90.00	85.68 ± 3.33

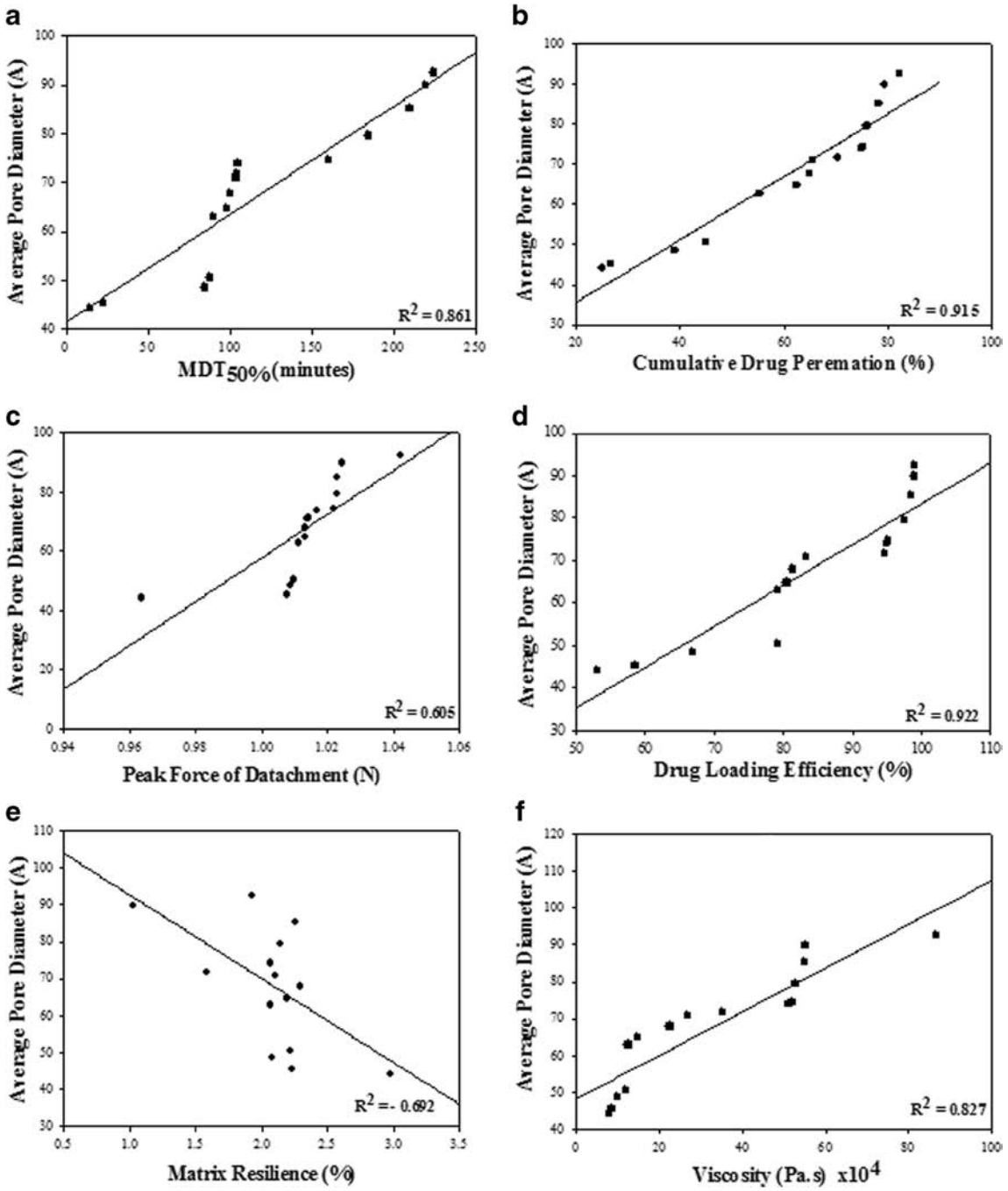

Fig. 1 Graphical representation showing direct and indirect linear mathematical relationships between β_D and (**a**) $MDT_{50\%}$, (**b**) CP_D, (**c**) F_{det}, (**d**)%DLE, (**e**) M_R and (**f**) η.

M_R ($R^2 = -0.794$) and η ($R^2 = -0.498$) (Fig. 2). The total formulation area which is occupied by pores is measured by the β_{SA}. Therefore, an increase in the magnitude of β_{SA} directly amplifies the degree of drug permeation and mucoadhesion to the mucosal site. On the contrary, a decline or elevation in β_{SA} can result in a respective increase or decrease in $MDT_{50\%}$, %DLE, M_R and η. Focusing on drug release measured with the $MDT_{50\%}$, it can be proposed that the release of drug molecules from the PCMS is not solely dependent on the β_D but also on the β_{SA}. This explains why the trend observed for the comparison of β_{SA} with the mean dissolution is opposite to the observed pattern for the β_D. Thus, a higher surface area of pore structures will result in lower $MDT_{50\%}$ indicative of rapid drug release and vice versa. Furthermore,%DLE appears to be more influenced by diameter of the pores than their surface area while with M_R, the impacts of both β_D and β_{SA} are similar. In addition, the viscosity of the blend seems to impact β_{SA} more than the β_D such that a decrease in blend thickness

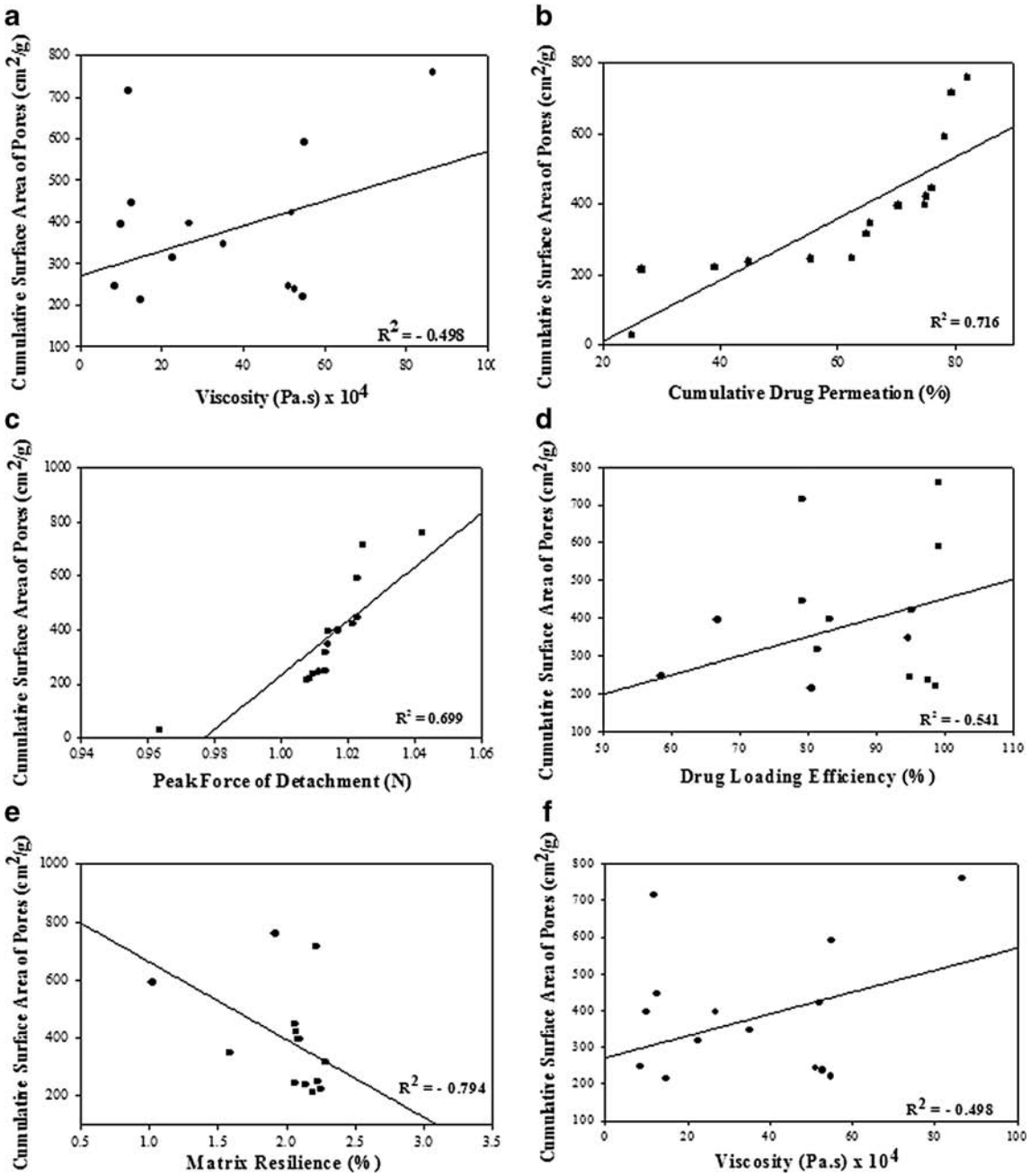

Fig. 2 Graphical representation showing the positive and negative linear mathematical relationships between ρ_{SA} and (**a**) $MDT_{50\%}$, (**b**) CP_D, (**c**) F_{det}, (**d**)%DLE, (**e**) M_R and (**f**) η.

generates a more porous formulation than its more viscous counterpart.

Experimental Techniques for the Explication of Fundamental Mechanisms of Formation and Action Utilizing the Optimized PCMS

Mechanism of Formation

Examination of Probable Shifts in Frequency Bands of Pertinent Functional Moieties. Distinctive vibrational frequencies of unique functional moieties of the pure polymeric, non-polymeric compounds and PS-Na were identified from generated FTIR spectra. Considered bands are enlisted in Fig. 3c (40–42). Subsequently, possible changes in band frequencies of these salient structural measures were compared between the FTIR spectra of the un-lyophilized blend and lyophilized PCMS (Figs. 3a and b with reference to that measured for the individual pure constituents (Fig. 3c). These spectra showed that both matrices are composed of multiple molecules as common bands overlapped while some shifted in terms of their frequencies and transmittance intensities. The spectra

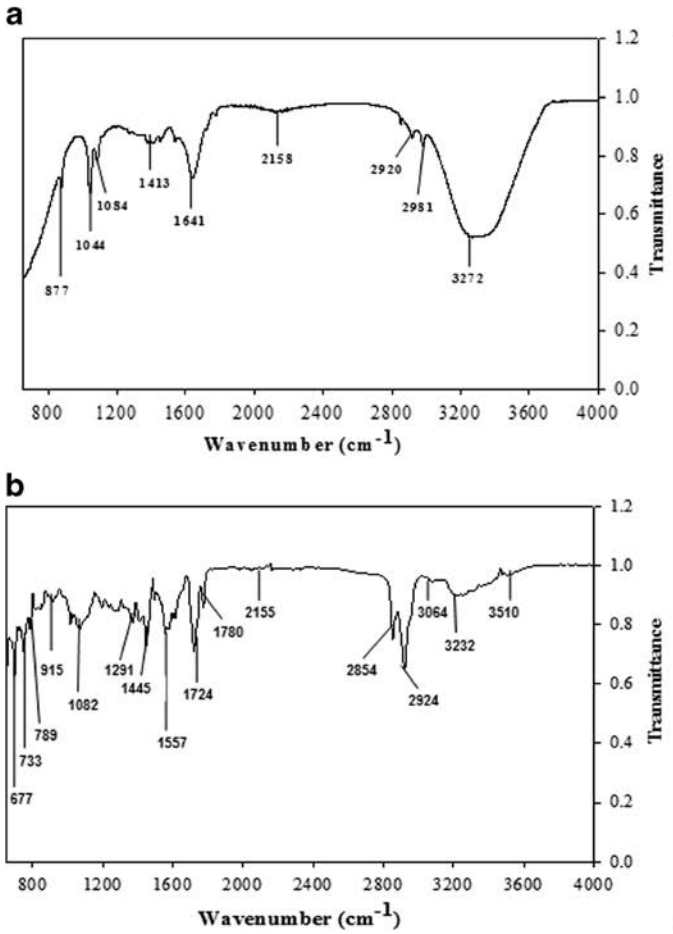

c

Compound	Functional Groups	Vibrational Frequencies (cm^{-1}) and Remarks
CHTS	$-CH_2OH$	2883 (CH stretch), 3442 (OH stretch), 1036 (C–OH stretch)
	-C-O-C	1158 (C-O-C cyclic stretch)
	$-NH_2$	3421 (NH stretch), 1611 ($-NH_2$ deformation)
MTH	$-CH_3$	2930 (CH stretch), 1449 (CH anti-symmetric deformation), 1371 (CH symmetric deformation)
	Cyclic CR_2OH	3264 (OH stretch), 1446 (C-OH in-plane bend), 682 (C-OH out-of-plane deformation)
GEL	$-CONH_2$	3334 (overlapping NH_2 and NH stretch), 1634 (C=O stretch), 1616 (NH_2 deformation), 1428 (C-N stretch)
	-CONHR	1542 (NH bend), 1250 (C-N stretch)
	$-CONR_2$ (*R= C atoms from a cyclic ring*)	620 (N-C=O bend)
	$-C-NH_3^+-COO^-$	3018 (H-bonded NH_2 and OH stretch), 1501 ($-NH_3^+$ deformation), 1495 (COO^- stretch)
	$-CH_2-$	2986 (C-H) stretch
PVA	$-CH_2-$	2952 (C-H stretch)
	$-CR_3OH$	3380 (OH stretch), C-OH (1101), 1086 (C-O-C stretch)
MS	$-CH_2-$ (multiple, linear chain)	2921, 2928 (C-H stretch)
	$-COO^- - Mg^{2+} - COO^-$	1579, 1577 (C=O stretch), 3481 (O^- Mg^{2+} stretch), 1122 (C-O stretch)
SP80	CR_3OH	3538 (OH stretch), 1098 (acyclic C-OH stretch), 1118 (cyclic C-OH stretch)
	C-O-C (cyclic)	1179 (C-O-C stretch)
	C=O	1744 (C=O stretch)
	-HC=CH-	3024 (=CH_2 stretch), 1645 (C=C stretch), 1178 (C-H out-of-plane deformation)
CARB 974	-COOH	3185 (H-bonded OH stretch), 1707 (C=O stretch), 942 (C-OH deformation), 756 (O-C=O bend)
ETH 10	CR_3OH (R = cyclic)	3533 (OH stretch), 1065 (C-OH stretch)
	-C-O-C (within a ring)	1380 (C-O-C stretch)
	$O-C_2H_5$	2980 (bending)
HEC	C-O-C (cyclic)	1439 (C-O-C stretch)
	C-O-C (linear)	1135 (C-O-C stretch)
	C-OH (cyclic)	1062 (C-OH stretch)
	$C-OC_2H_5$	3462 (OH stretch), 2921 (C-H stretch)
PS-Na	C_6H_6	3154 (C-H stretch), 1693-2018 (weak C-H from the benzene/phenyl ring; overtones and combinations)
	$R_2-C=O$	1693 (C=O stretch)
	R-NH-	3341 (NH stretch), 1159 (C-N stretch), 697 (NH deformation)
	$-O^-Na^+$	1401 (stretch)

Fig. 3 A presentation of the (**a**) optimized, un-lyophilized homogenous blend FTIR spectra, (**b**) optimized, lyophilized PCMS FTIR spectra and (**c**) vibrational frequencies of functional moieties of the pure individual compounds constituting the PCMS.

of the un-lyophilized blend (Fig. 3a) displayed a broad band at 3272 cm^{-1} attributable to the overlap of OH and NH_2/NH or C-OH stretching vibrations present in all components and/or the influence of multiple intra- and intermolecular hydrogen bonds due to the introduction of the EtOH and DW for the dispersions of the solutes. This can also be as a result of hydration of the component compounds or hydrolysis of the $C-O^- Na^+$ bond from PS-Na. The bands at 2981–2920 cm^{-1} could be related to C-H stretching from the methylene ($-CH_2-$) or ethoxide ($-O-C_2H_5$) functional groups and C-H stretching/bending of alkyl groups respectively. The peak at 2158 cm^{-1} can be an extension of the effects of the C-H and $O-C_2H_5$ vibrations which was influenced by the introduction of EtOH and DW. The peaks recorded at 1641–1413 cm^{-1} are characteristic of overlapping vibrations from C-OH and N-H bending; NH_2 and NH_3^+ deformations; C=O, C-N, C=C, C-O-C, COO^- and O^-Na^+ stretches as well as weak phenyl C=C overtones from the different compounds. Furthermore, the bands recorded at 1084–1044 cm^{-1} are notable for interactions of C-O, C-N, C-OH (acyclic), C-OH and C-O-C (linear) stretching vibrations as well as C-H (out-of-plane) deformations. Finally, the band recorded at 877 cm^{-1} could be associated with non-destructive, reversible, physical perturbations of the structural backbones of some components due to solvation with functional group vibrations such as N-H and C-OH deformation, O-C = O and N-C = O bending occurring (38–41).

Several peaks were observed with the spectra generated for the lyophilized PCMS due to the contributive influences of its components. Notable peaks were at 3510–3232 cm^{-1} associated with OH, NH and NH_2 stretches; 3064–2854 cm^{-1} attributable to interactive C-H (cyclic or linear), intramolecular hydrogen bonded NH_2 and OH stretch, $O-C_2H_5$ bending; 2155 cm^{-1} due to weak C-H combinatorial overtones within the benzene ring; 1780–1724 cm^{-1} due to C = O, C = C stretching, $-NH_3^+$ and NH_2 deformations, N-H bending vibrations; 1557–1445 cm^{-1} consequent to COO^-, C-O-C (linear/acyclic), C-N stretching, C-OH in-plane bend, $C-O^-$ and CH deformation; 1291–1082 cm^{-1} resulting from C-OH (acyclic and cyclic), C-O-C (acyclic), C-N stretching; 915–677 cm^{-1} associated with C-OH, NH deformations, O-C = O, N-C = O and C-OH (out-of plane) bending (38–41). Furthermore, the absence of the conspicuous broad band observed for the un-lyophilized blend (Fig. 3a) between

3200 cm^{-1} and 3600 cm^{-1} reflects the absence of OH and NH_2 from the presence of water molecules due to lyophilization.

The spectral patterns the blend and PCMS highlight that structural transitions were physical in nature and that the shifts recorded for characteristic peaks were due to the reversible interactions among the constituting compounds. Also, formation of reversible, non-destructive hydrogen bonds during the solute dispersion process with EtOH/DW combination can influence the shifts in measured peak frequencies. Furthermore, the process of lyophilization may have initiated physical interactive intra- and intermolecular forces such as the van der Waals, electrostatic, ionic which may also instigate observed frequency shifts. Overall, the processes of homogenization, pre-freezing and lyophilization employed in the fabrication of the PCMS formulation did not irreversibly distort the chemical structure of the constituting compounds. In other words, each constituting compounds retained their original physical qualities during the construction of the PCMS.

Changes in Thermal Quantities Due to the Application of Heat Energy. The thermal transitions which occurred within the blend and PCMS lattices were measured in terms of the glass transition (T_g), the reversible heat flow due to changes in the magnitude of the heat capacity complex (C_p-complex) (ΔC_p) and melting (T_m) which is related to irreversible heat flow corresponding to total readings. The T_g and T_m of each excipient and PS-Na were separately determined utilizing C-DSC to enhance logical comparative examination. T_g values in°C were 55.08, 44.11, 60.99, 48.56, 80.04, 60.01, 67.96, 101.02, 87.97, 85.99 while T_m in°C were 222.54, 212.89, 228.87, 210.12, 202.12, 260.33, 218.47, 228.68, 234.55, 200.05 for CHT, MTH, GEL, PVA, MS, SP 80, CARB 974, ETH 10, HEC, PS-Na respectively. TM-DSC revealed and distinguished important hidden and overlapping thermal events not identified with C-DSC. Figure 4 shows typical C-DSC and TM-DSC profiles for the blend and PCMS respectively displaying multi-transitional thermal behaviours as several T_g (endothermic) and T_m (exothermic) peaks were recorded (Table VIII) indicating the presence of multiple compounds within the matrix and the absence of any irreversible chemical transformations during PCMS preparation. However, a comparison of T_g and T_m values for each compound mentioned earlier with that of the blend and/or PCMS revealed that the combination of the compounds and the inclusion of DW and EtOH resulted in shifts in the T_g and T_m (Table VIII). This can be attributed to the fact that the presence of multiple compounds and additionally water/ethanol within the PCMS and blend matrices respectively influenced the physical processes governing non-destructive structural mobility related to changes in heat magnitude. The presence of interactive intra- and intermolecular hydrogen bonds can also be a contributing feature. Thus, these factors can influence the extent of polymeric/non-polymeric chain mobility due to endothermic (T_g) or exothermic (T_m) responses and changes in randomness within each lattice which can then impact dynamic dimensional changes as a result of chain realignments (glass transition), bond breakages and chain deformations (melting) affecting PCMS or blend thermodynamic stability resulting in the variations in magnitudes of thermal quantities (Table VIII). Furthermore, the total heat energy required for the observed T_g and T_m transitions were mathematical integrated and the blend had higher values (200.16 mJ) than the PCMS (10.08 mJ) implicating the intensity of the multiple hydrogen bonds (due to solvation) within the blend as explained earlier which have to dissociated before any macroscopic dimensional entropic changes could be realized.

Gravimetric Changes in Samples During the Fabrication Process of the PCMS. The changes in weight at the different phases (W_0–W_5) of designing the PCMS are illustrated with Fig. 5. Weight transitions were four phased namely an initial increase: W_0-W_1, a moderately steady segment: W_1 - W_2, a slight increase: W_2 - W_3 followed by a sharp decrease at W_4-W_5. An increase in weight observed from W_0 (181.50 ± 3.45 mg) to W_1 (1010.51 ± 7.06 mg) was due to changes in densities/masses/volumes of the employed additives - span 80, DW and EtOH introduced to form the homogenous blend. It was observed that W_1 was relatively maintained over the blend curing phase which yielded W_2: 1109.89 ± 5.11 mg. This slight mass changes between W_1 and W_2 can indicate that some level of polymeric swelling and enhanced physical homogenization occurred but did not result in any chemical transitions as no drastic changes in weight was notable. The minor increment in weight observed from W_2 (1109.89 ± 5.11 mg) to W_3 (1112.69 ± 4.89 mg) could be associated with the effects of freezing on the homogenous blend. Freezing can initiate solute-solute/solute-solvent/solvent-solvent intermolecular coalescence which can result in molecular packing and volumetric shrinkage leading to the generation of an orderly crystalline structure and a possible change in mass and density of the frozen blend. Weight reduction from W_3 (1112.69 ± 4.89 mg) to W_4 (568.50 ± 2.22 mg) and finally W_5 (175.30 ± 4.01 mg) is related to the process of sublimation of the frozen solvent molecules leaving behind pores within the matrix. A close relationship existed between the starting mass (W_0) and the final mass of the PCMS (W_5) suggesting that the whole process of PCMS fabrication was physical in nature and that matter was neither created nor destroyed (absence of chemical transitions) as no noteworthy changes in weight magnitude was observed.

Changes in Matrix Physicomechanical Texture. Transitions in matrix textural properties were measured with M_F and ϵ_D which showed that the different phases of the PCMS production involved significant changes in physicomechanical quantities. In this case, M_F can be related to the PCMS matrix

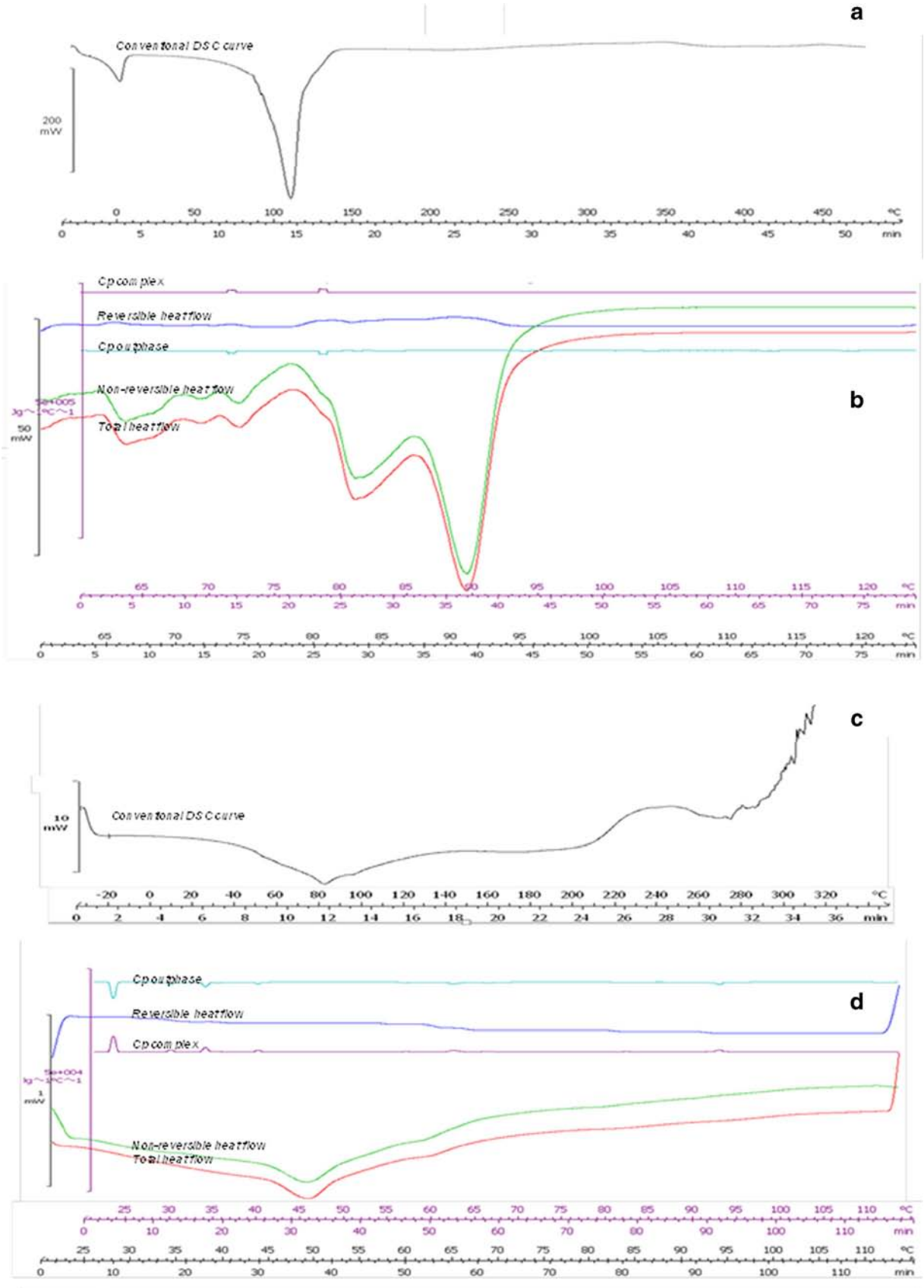

Fig. 4 Typical illustrations showing: (**a**) C-DSC, (**b**) TM-DSC thermograms of the un-lyophilized blend and (**c**) C-DSC, (**d**) TM-DSC thermograms of the lyophilized PCMS.

Table VIII Temperature Changes Revealing Salient Multi-Transitional Thermal Events Evidenced by Diverse Endothermic and Exothermic Inflection Peaks

Thermal events	Homogenous blend	PCMS
Glass transition temperature (°C)	−17.54	24.11
	−14.25	28.49
	30.44	33.00
	64.55	39.61
	71.52	56.04
	89.59	61.00
	190.50	65.42
	202.00	83.00
	210.11	94.01
	215.98	161.54
	218.00	177.22
	221.15	182.00
	262.02	205.11
	264.08	227.00
	307.59	–
	310.09	–
Melting temperature (°C)	−14.09	23.15
	30.55	45.50
	36.00	–
	63.00	59.91
	69.00	80.05
	73.11	180.22
	81.50	218.04
	89.84	–
	173.30	–
	238.52	–
	252.99	–
	264.00	–
	342.01	–

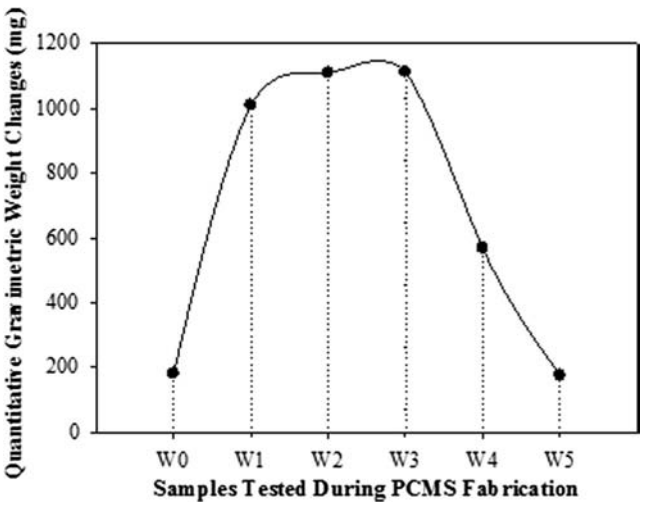

Fig. 5 Quantification of gravimetric changes at strategic points during the fabrication of the PCMS ($n = 3$ and Standard Deviation ≤8.95 mg in all cases).

resistance to the penetration of an external stress while ϵ_D can be described as energy dissipated during this process. An inverse relationship between M_F and ϵ_D was noted implying that firmer matrices required higher energy quantities to overcome intrinsic interactions responsible for matrix stiffness during the penetration of an external force resulting in the external dissipation of reduced energy levels. The unhydrated blend of PS-Na and additives used for the production of the PCMS had the lowest M_F (1.029 ± 0.051 N/mm) and highest ϵ_D (0.062 ± 0.007 J) which suggests that the inherent resistance of the dried samples to penetration of the externally applied force was minimal resulting in the dissipation of higher energy quantity showing that molecular interactions amongst the constituents of this sample were nominal and that the system was in a disordered state. With the introduction of DW (WMD) and EtOH (EMD), significant increases in M_F (WMD: 15.887 ± 1.101 N/mm; EMD: 9.087 ± 0.593 N/mm) and ϵ_D (WMD: 0.022 ± 0.001 J; EMD: 0.031 ± 0.003 J) compared to the dry mix were observed indicating that dried components were significantly hydrated resulting in physical interactions between solvent and solute molecules, co-particulate dispersion and distension to generate a gel-like, inter-tangled, solute-solvent network which posed as a barrier to the externally applied force. The combination of WMD and EMD with the inclusion of the surfactant, span 80, which formed the un-lyophilized homogenous blend before curing had a higher M_F (20.591 ± 1.224 N/mm) and lower ϵ_D (0.014 ± 0.001 J) relative to WMD or EMD individually. This can be associated with the fact that span 80 enhanced interfacial homogenization resulting in the formation of a stable, colloidal homogenate prior to curing. Furthermore, curing of the homogenous blend appears to have some positive impact on blend thickness as an increase in M_F (22.616 ± 0.897 N/mm) and a decrease in ϵ_D (0.012 ± 0.004 J) compared with the uncured blend was observed.

Therefore, the curing process can be said to enhance multi-particulate swelling and inter-tangling and eventually facilitate the formation of an ordered porous matrix template. Furthermore, a sharp decline in M_F (4.192 ± 0.548 N/mm) and increase in ϵ_D (0.048 ± 0.001 J) values were obtained for the lyophilized PCMS implying that the sublimation process that took place during lyophilization returned the matrix into its dry state but with some changes which occurred within its internal matrix structure evidenced by relating the M_F (1.029 ± 0.051 N/mm) and ϵ_D (0.062 ± 0.007 J) values of the unhydrated dried blend of PS-Na and excipients. These notable changes can be attributed to the introduction of a stable porous structure comprising of the pores and interconnectors which could serve as relevant barriers to mechanical penetration resulting in higher M_F and lower ϵ_D values compared

with the unprocessed mixture of the dry components. Overall, the stages involved in the construction of the PCMS involved salient physicomechanical textural transitions.

Mechanism of Action

FTIR Frequency Transitions During the PCMS Performance

Comparatively, each test samples (X_{0h}, X_{1h}, X_{2h}, X_{4h} and X_{8h}) generated varied trends of vibrational frequencies based on comparing the unhydrated PCMS to the hydrated samples over a specified period. Table IX presents the measured bands showing the shifts (with respect to the unhydrated PCMS, X_{0h}) which occurred during the dissolution processes of the tested formulations over time (X_{1h}, X_{2h}, X_{4h} and X_{8h}). The observed band shifts presented in Table IX may indicate that hydration of the PCMS in simulated saliva perturbed its backbone but did not bring about major cut off transitions. Band changes in this regard can refer to shifts of existing ones such as OH, NH, NH_2, C-H, H-bonded NH_2 and OH stretching and O-C_2H_5 bending (3510–2854 cm^{-1}: X_{0h}) bands gradually shifted to 3449–2852 cm^{-1} (X_{1h}), 3275–2852 cm^{-1} (X_{2h}), 3269–2852 cm^{-1} (X_{4h}) and then 3268–2852 cm^{-1} (X_{8h}). The immobilization of the weak C-H overtones present within the benzene ring of PS-Na (2325–1982 cm^{-1}) was also observed. The band shifts displayed by all hydrated samples (X_{1h}, X_{2h}, X_{4h} and X_{8h}) in comparison to the unhydrated reference (X_{0h}) can be linked to the formation of intra- and inter-molecular hydrogen bonding with water molecules aiding the process of solvation. Also, the presence of electrolytes within the buffered dissolution medium may initiate some level of reversible ionic bonding which potentially destabilizes the matrix stable network bringing about observed shifts in vibrational frequencies. In addition, it was noted that the stretching frequency was essentially the same for X_{4h} and X_{8h} indicating that the process of solvation was complete between the 4th and 8th hour. Overall, the PCMS can be described as stable and sturdy because despite the progressive process of matrix hydration and dissolution, each specimen retained its original, unhydrated chemical composition. In other words, the additives and PS-Na remained chemically intact through the process of wetting, dissolution and disintegration as all analyzed samples generally retained the key functional moieties.

Viewing of Matrix Surface Morphology Over Exposure Time

The scanning electron micrographs (Fig. 6) obtained for each hydrated sample in comparison with the unhydrated one changed steadily as exposure time increased. Obtained

Table IX Shifts in the Vibrational Frequencies of Relevant Functional Moieties of the Hydrated Samples with the Unhydrated PCMS Formulation as a Reference Point

Key functional groups vibrational frequencies	Formulation description				
	X_{0h}	X_{1h}	X_{2h}	X_{4h}	X_{8h}
OH, NH, NH_2, stretching	3510	3449	–	–	–
	3252	3261	3275	3269	3268
C-H (cyclic or linear), H-bonded NH_2 and OH stretching and O-C_2H_5 bending	3064	–	–	–	–
	2924	2920	2920	2916	2918
	2854	2852	2852	2852	2852
Weak C-H overtones	2155	2162	2162	2165	–
	–	1982	1982	1982	1982
C=O, C=C stretching, $-NH_3^+$ and NH_2	1780	1741	1738	1741	1738
deformation and N-H bending	1724	1635	1640	1640	1640
COO^-, C-O-C, C-N stretching, C- OH bend,	1557	1539	1540	1540	1542
C-O^- and CH deformations	1445	1463	1463	1463	1455
	–	1413	1415	1415	1413
C-OH, C-O-C (acyclic), C-N stretching	1291	1374	1376	1376 1351	1377
	–	–	1314	1312	1310
	–	1245	1240	1242	1240
	1082	1072	1054	1057	1056
C-OH, NH deformations, O-C=O, N-C=O and	915	919	919	915	921
C-OH bending	789	882	883	879	887
	733	818	818	816	848
	–	723	717	723	713
	677	663	668	667	–

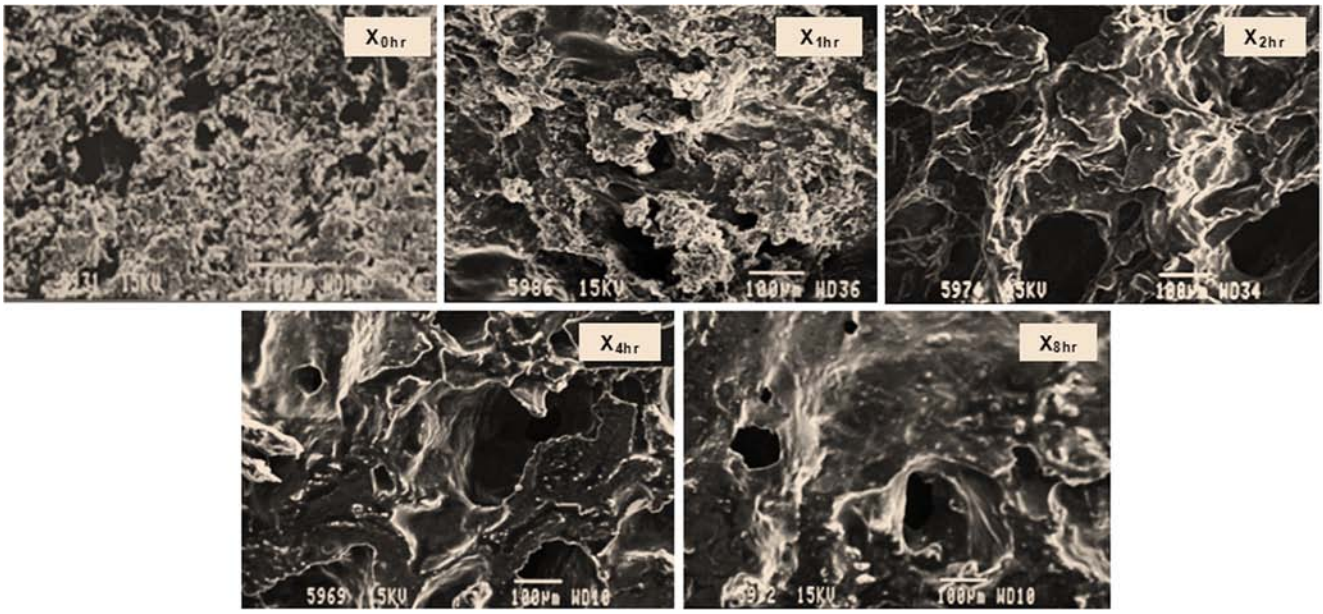

Fig. 6 Scanning electron micrographs showing the time dependent changes in the matrix surface topography (magnification 1000×).

micrographs show that the porous network collapsed as the duration of exposure to the dissolution media increased. At the first hour (X_{1h}), the well-structured unhydrated porous structure (X_{0h}) began to open up, the collapse of pore interconnectors was initiated and larger undefined pores were formed. As hydration progressed to 2 h post-exposure (X_{2h}), the porous network collapsed gradually and interconnectors merged and got less visible and more formless. Also, the formation of undefined globules due to the interactive influx of water molecules is notable at 2 (X_{2h}) and 4 h (X_{4h}). Furthermore, structures that can be denoted as gullies due to matrix erosion and collapse of the structured porous network was evident for X_{2h}, X_{4h} and X_{8h}. At the 8 h (X_{8h}), a near complete collapse of porous structure was observed. Therefore, an inference that the hydration of the PCMS resulted in the collapse of its ordered porous network due to matrix loosening that gradually will lead to progressive drug release and erosion.

Matrix Gravimetric Changes Due to Hydration

Matrix mass loss was consistent with time post exposure to the dissolution media. Alternatively, the residual matrix reduced in weight as the duration of hydration increased (Fig. 7a). This implies that the process of matrix hydration which activated and conserved the collapse of the ordered porous network (Fig. 6) led to matrix solvation and overall mass loss as the time of exposure to the dissolution media increased. The relationship between matrix erosion and drug release was mathematically explored and interestingly, a linear relationship ($R^2=0.938$) indicating a direct dependence of these two mechanisms on each other was noted (Fig. 7b). Furthermore, it can be proposed that the PS-Na molecules were entrapped and well distributed within the pores and interconnectors of the PCMS such that they are only be liberated once the porous network was disrupted.

Matrix Textural Alterations

The graphical representation of the changes in the numerical values of M_F and ϵ_D for each sample is illustrated with Fig. 8a and b respectively. In addition, Fig. 9 depicts the changes in the quantities of the measures of physicochemical texture which occurred for each sample over time.

M_F, measuring the matrix resistance to external force penetration increased for X_{1h} (22.790±1.223 N/mm) relative to unhydrated X_{0h} (4.264±0.500 N/mm) and as hydration progressed with time it decreased consistently (X_{2h}=14.376±0.980 N/mm; X_{4h}=11.912±0.775 N/mm; X_{8h}=9.4820±1.014 N/mm) but all values were higher than that of dry X_{0h}. Based on the observed increase in M_F from X_{1h} to X_{8h} compared to the dry X_{0h}, an inference that a level of swelling occurred coupled with the plasticizing effects of water coming to play giving rise to a matrix with increased tortuosity and resistance to external force penetration can be put forward. Furthermore, the notable subsequent decline in the magnitude of M_F for X_{2h}, X_{4h} and X_{8h} with reference to X_{1h} can be due to matrix loosening, collapse of ordered porous structure and gradual erosion occurring concomitantly as wetting progressed. Consequently, the magnitude of the force of penetration reduces as the matrix barrier capacity and penetration distances are minimized. This proposition is further fortified by the illustration in Fig. 9 as the magnitude of the

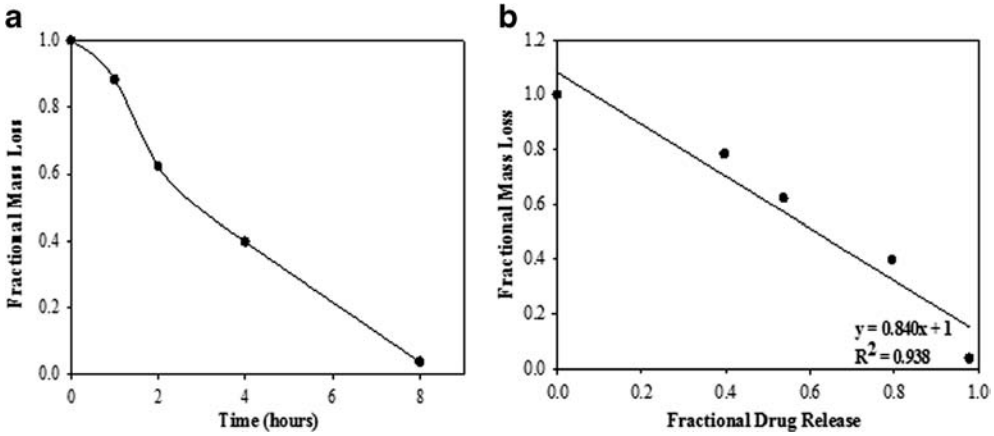

Fig. 7 Graphs showing: (**a**) Gravimetric changes in PCMS matrix for the duration of exposure to the dissolution medium ($n = 3$ and Standard Deviation ≤0.02 in all cases) and (**b**) Linear relationship between fractional drug release and fractional mass loss.

penetration force and distance decreased as hydration time increased from X_{1h} to X_{8h}. With ϵ_D, a measure of energy dissipated to the environment, a decrease was observed for all hydrated samples: $X_{1h} = 0.0230 \pm 0.0010$ J; $X_{2h} = 0.0290 \pm 0.0002$ J; $X_{4h} = 0.0350 \pm 0.0004$ J and $X_{8h} = 0.0420 \pm 0.0001$ J compared to the dry $X_{0h} = 0.0489 \pm 0.0003$ J. This noteworthy trend indicates that less energy was externally liberated during the application of an external force due to the fact that more energy is being used up within each matrix to overcome internal barriers introduced by the presence of plasticizing water and swellable polymeric molecules. Comparing X_{0h} to X_{1h}, ϵ_D decreased sharply due to the initiation of matrix wetting and swelling but as hydration progressed, ϵ_D gradually increased and was highest for X_{8h} which can be explained by the processed of system disentanglement and disintegration setting in. The magnitude of ϵ_D for unhydrated X_{0h} was highest (0.0489 ± 0.0003 J) showing that it presented with minimal hindrances to penetration resulting in a reduction in the magnitude of performed work and an elevation in the level of energy dissipated to the environment.

Furthermore, the changes in matrix porosity depicted by the undulating peaks in Fig. 9 were computed as a textural quantity described as "average drop offs" (red and green arrows). It was observed that these values dropped from 15.48 (X_{0h}) to 2.58 (X_{1h}), 0.89 (X_{2h}), 0.16 (X_{4h}) and 0.08 (X_{8h}) showing a decrease in the orderliness of the matrix structure. This further substantiates the relationship between matrix hydration, porous structure configuration and physicomechanical textural transitions.

The Application of an *In Silico* Approach to Elucidate the Mechanisms of Configuration and Function of the PCMS Formulation

Prediction of the Mechanism of PCMS Configuration

Generated computational models showed that the formation of the homogenous blend was initiated by solute (CHTS, MTH, GEL, PVA, CARB 974, SP 80, ETH 10, HEC, MS, PS-Na) and solvent (EtOH and DW represented as stars in Fig. 10) interactive dispersions which gave rise to hydrophilic pockets with different polymeric and non-polymeric multimolecular strand associations as well as dispersed DW (free space) (Fig. 10a–i), EtOH (free space) and PS-Na molecules (represented by square dots) within the mixed matrix (Fig. 10a). The PS-Na molecules were located in close proximity to the hydrophilic pockets and in close association with other solute-solvent components. Also, the PS-Na molecules

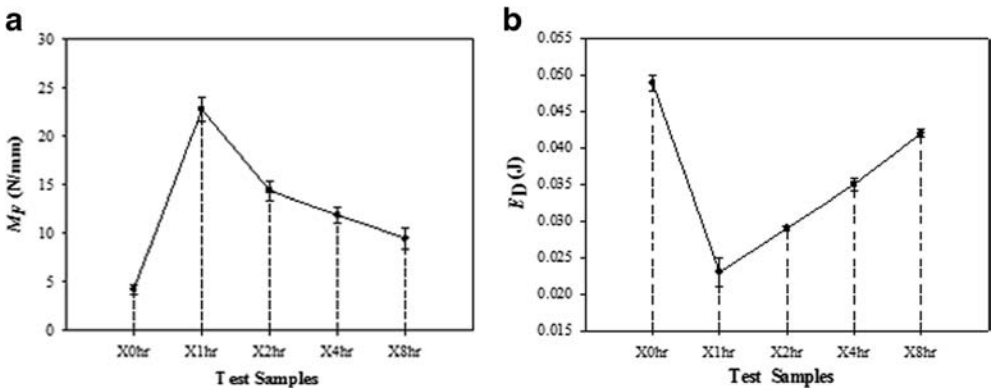

Fig. 8 Plots depicting changes in matrix physicomechanical texture due to hydration measured as: (**a**) matrix firmness and (**b**) energy of matrix distortion.

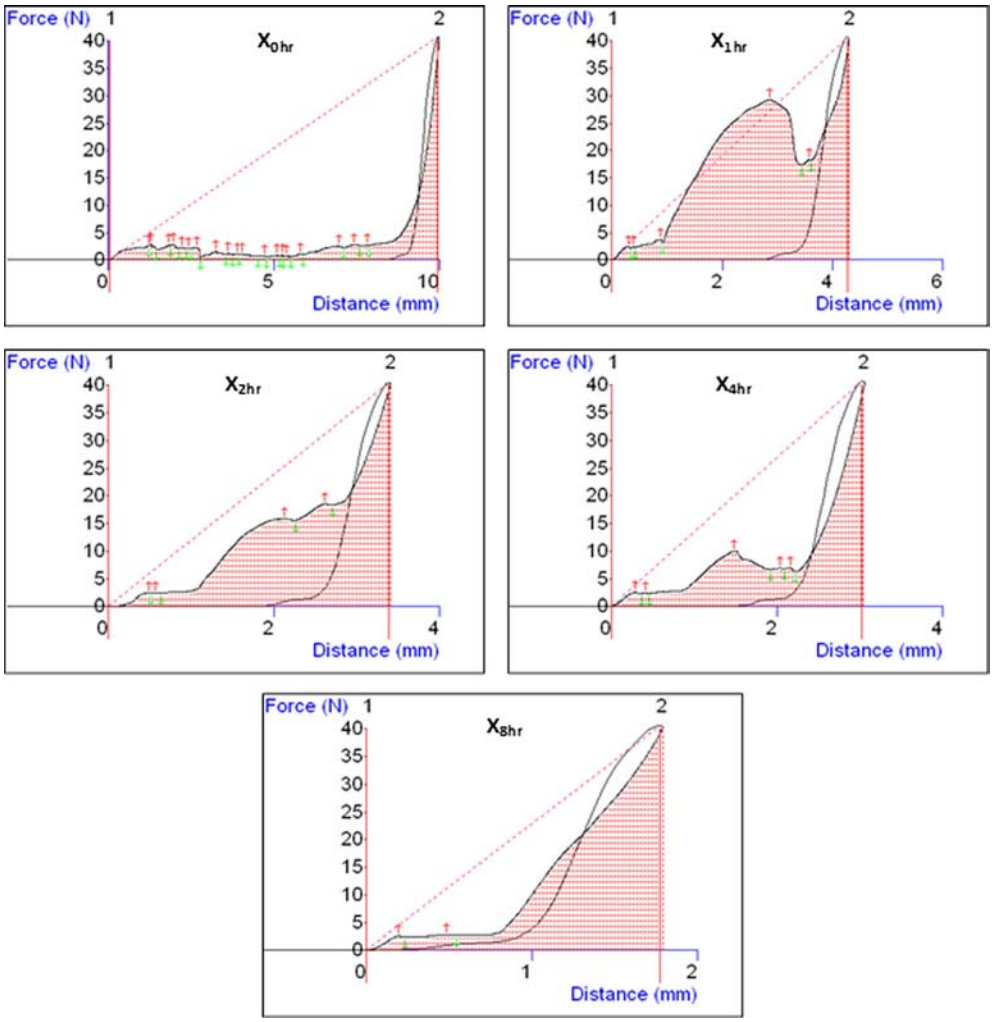

Fig. 9 Profiles showing the changes in matrix texture over time due to hydration.

displayed particular interactions with GEL molecules (eccentric circular dots) which may be attributed to its high level of hydrophilicity (Fig. 10a(ii)). Fig. 10a(iii) models a PS-Na-loaded homogenous blend prior to lyophilization. Interactions between the solute particles and DW-EtOH solvent medium were prominent and mainly of the hydrophilic type. This resulted in the formation of solute-solvent dispersions due to layering of the solvent components. Hydrophilic-natured pockets developed around carboxyl and hydroxyl entities of the polymeric and non-polymeric solute components without strand twisting which are indicative of physical, non-destructive transitions (Fig. 10b). It was noted that solute-solvent interactions occurred in different orientations with some areas showing higher solvent clusters than some other regions due to the varying affinities of the solute centres and PS-Na molecules for the solvent functional groups (Fig. 10c). The generated model was able to visualize the formation of single and multiple cavities resulting from the associative physical interactions between the solute and solvent molecules within the homogenous blend milieu (Fig. 10d). These cavities appear to be prerequisites to the formation of the stable porous structures as well as possibly functioning as interfaces for the attachment of drug molecules.

Furthermore, the multiple cavities were observed to be associated with the multiple solute strand interaction giving rise to inter-strand cavities (Fig. 10e): (i) drug-loaded, homogenized blend, (ii) multiple strands undergoing physicochemical interactions along with drug molecules (as squared dots), (iii) physicochemical interactive associations (represented as broken and solid lines) between solute-solute strands interconnectors, (iv) a foot-print view of the associations and channel cavity and (v) a three-dimensional view of inter-strand networked channels (ordered porous structure) with drug molecules loaded unto the matrix. In addition, the model showed that interconnection of the multiple cavities occurred and this resulted from the multiple solute strands undergoing multi-link physical interactions along with the drug molecules to form channels (in the angstrom size range) indicative of the ordered porous structure (including the pores and interconnectors) of the PCMS matrix (Fig. 10f).

Overall, the schematic in Fig. 10g depicts the computationally modelled phases of fabrication of the PS-Na-loaded

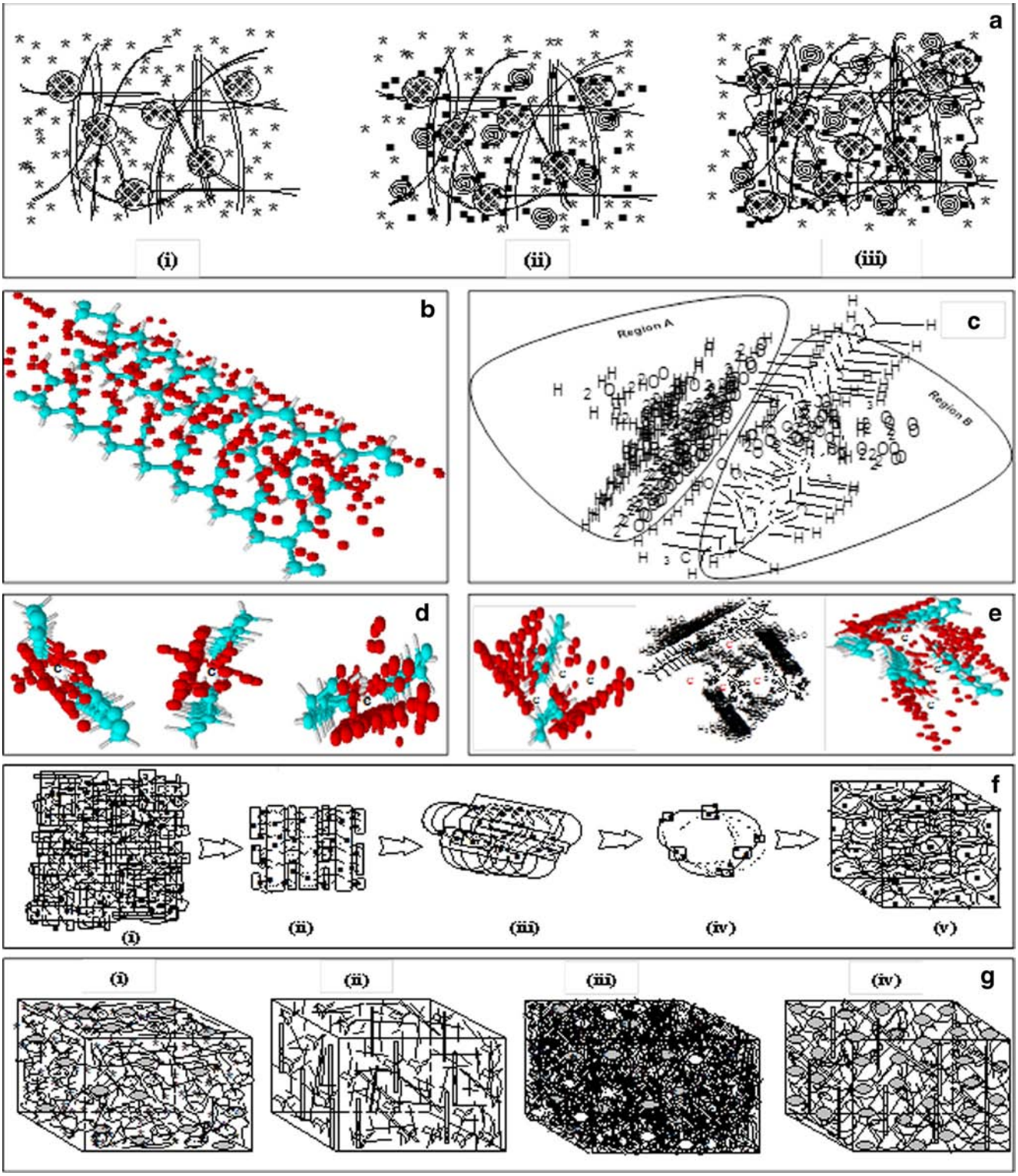

Fig. 10 *In silico* models displaying the: (**a**) processes of formation of the drug-loaded homogenous blend, (**b**) interaction between solvent centres (*red circles*) and solute strands (*greenish circles*) forming hydrophilic-natured pockets (*off-white spaces*), (**c**) layering due to strong hydrophilic solute-solvent interactions (Region A) and scattered solvent molecules (Region B) around lesser affinity moieties, (**d**) solute-solvent interactions resulting in the formation of cavities (portions labeled 'c'), (**e**) multiple solute strands in interaction with solvent molecules resulting in the evolution of inter-strand multiple cavities ('c'), (**f**) formation of interconnected cavities forming the channels, (**g**) summary of the stages involved in the fabrication of the ordered porosity-controlled matrix.

PCMS: (i) drug loaded water-based co-particulate dispersion showing several solute strands, drug molecules (grey circles) undergoing hydrophilic physicochemical interactions (white circles) and molecules of the water (star-shaped entities)

scattered within the matrix, (ii) the ethanol based co-particulate dispersion with the solutes depicted as broken lines and elongated double lines, ethanol molecules as y-shaped figurines scattered in the preparatory matrix, (iii) a mixture of (i) and (ii) with span 80 (reduction of interfacial tension) to form the homogenous co-particulate blend characterized by as increased volume density of the constituents, (iv) the freeze-dried or lyophilized matrix devoid of free floating water, water pockets, ethanol and ethanol-water associative entities which gave rise to a homogenized and ordered porous matrix showing solute strands from both the water-based and ethanol-based co-particulate dispersions origins as well as evenly distributed drug molecules and other associated adds-up of the blend (physical interaction).

Paradigms Validating the Mechanism of Performance

Computational modeling predicted that the PCMS matrix functioned basically by undergoing a compressive break-up of the ordered porous structure illustrated with Fig. 11a. Significant changes in energy levels during the construction and performance of the PCMS formulation were observed employing the *in silico* models. The modeled internal energy (E) was higher for the lyophilized PCMS than for the unlyophilized homogenous blend. This is indicative of a stable, less perturbed PCMS milieu with minimal entropy changes. The process of matrix breakdown was characterized by regressive energy decay over time which can be related to a reduction in system internal stability due to extrication and an upsurge in system entropy levels (Fig. 11b and c).

Molecular Mechanics Assisted Model Building and Energy Refinements

Molecular mechanics energy relationship (MMER), a method for analytico-mathematical representation of potential energy surfaces, was used to provide information about the contributions of valence terms, noncovalent Coulombic terms, and noncovalent van der Waals interactions for the polymer-polymer and polymer-mucin interactions. The MMER model for potential energy factor in various molecular complexes can be written as:

$$E_{molecule/complex} = V_{\sum} = V_b + V_\theta + V_\varphi + V_{ij} + V_{hb} + V_{el} \quad (7)$$

where, $V_{\sum}$ = total steric energy for an optimized structure, V_b = bond stretching contributions, V_θ = bond angle contributions, V_φ = torsional contributions, V_{ij} = van der Waals interactions due to non-bonded interatomic distances, V_{hb} = hydrogen-bond energy function and V_{el} = electrostatic energy.

In addition, the total potential energy deviation, ΔE_{Total}, was calculated as the difference between the total potential energy of the complex system and the sum of the potential energies of isolated individual molecules, as follows:

$$\Delta E_{Total(A/B)} = E_{Total(A/B)} - \left[E_{Total(A)} + E_{Total(B)}\right] \quad (8)$$

The molecular stability can then be estimated by comparing the total potential energies of the isolated and complexed systems. If the total potential energy of complex is smaller than the sum of the potential energies of isolated individual molecules in the same conformation, the complexed form is more stable and its formation is favored [43].

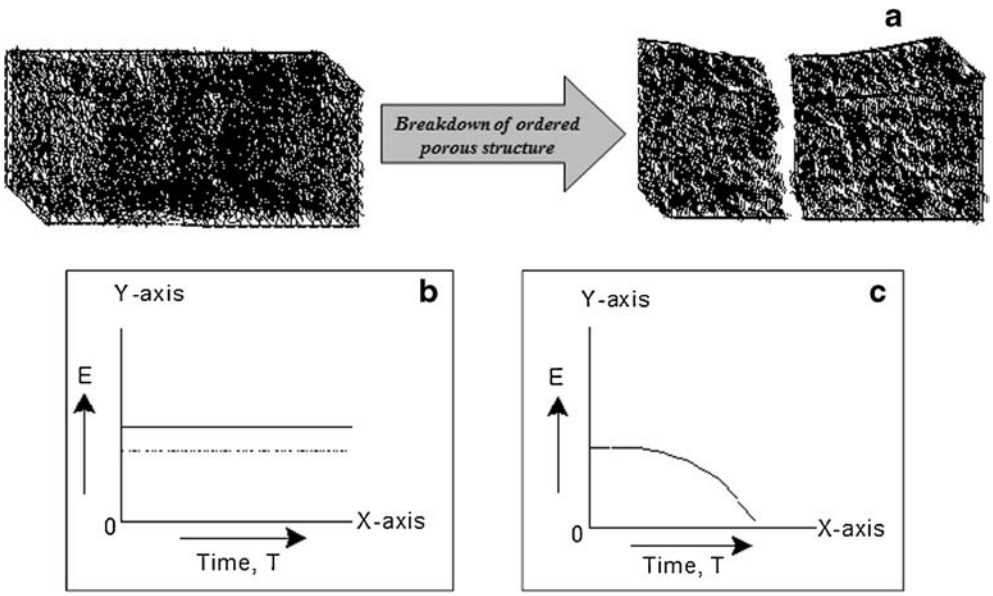

Fig. 11 Computationally modeled illustrations showing: (**a**) compressive disruption of the ordered porous structured matrix, (**b**) averaged typical energy, E against time, T of the porous matrix (*solid line*) and energy of the homogenized blend (*broken lines*) and (**c**) energy decay over time in a regressive pattern.

Polymeric Co-Blending to Achieve Optimized PCMs Configuration

To assess the interaction and performance profile of the matrix components, the modeling paradigm was divided into three sub-groups viz. 1) EMD consisting of CHT and EC represented by Eqs. 9–11; 2) WMD consisting of PVA, PAA, HEC and GEL represented by Eqs. 12–16; and 3) finalized PCMS configuration consisting of combined EMD and WMD components represented by Eqs. 9–17.

$$E_{CHT} = 11.410\ V_{\sum} = 1.293\ V_b + 7.265\ V_\theta + 9.796\ V_\varphi + 7.211\ V_{ij} - 14.155\ V_{el} \quad (9)$$

$$E_{EC} = 51.310\ V_{\sum} = 2.172\ V_b + 13.373\ V_\theta + 9.05\ V_\varphi + 3.696\ V_{ij} + 23.01\ V_{el} \quad (10)$$

$$E_{EMD} = 9.424\ V_{\sum} = 2.172\ V_b + 13.373\ V_\theta + 9.05\ V_\varphi + 3.696\ V_{ij} + 23.01\ V_{el}; \quad (11)$$

$$\Delta \mathbf{E} = -53.296\,\text{kcal/mol}$$

In case of ethanol-based multi-elemental dispersion (EMD) in silico architecture, the polymeric components, chitosan and ethylcellulose, displayed favourable interaction profile with a –ve energy of binding ($\Delta E = -53.296$ kcal/mol). The

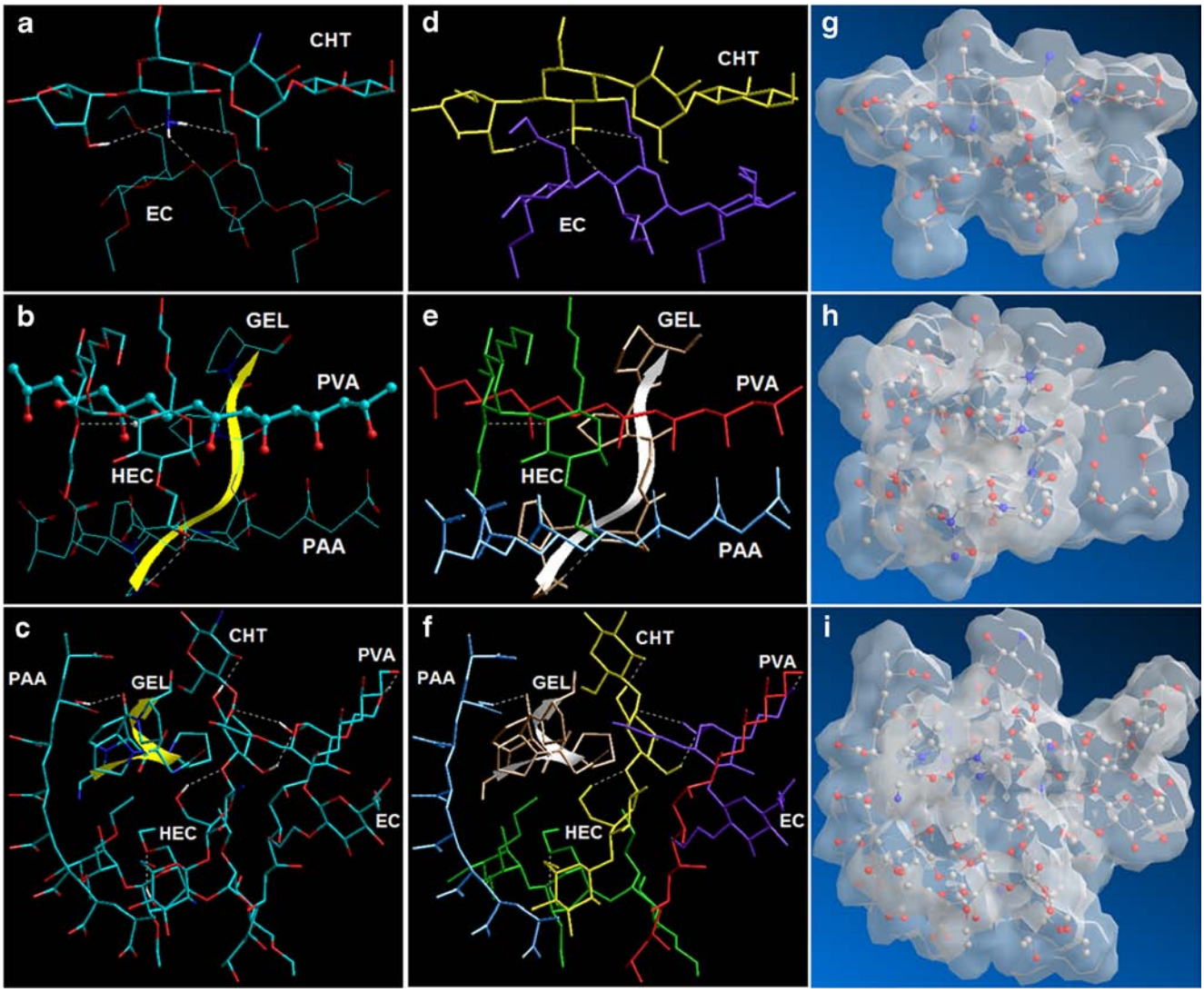

Fig. 12 Visualization of geometrical preferences of (**a**) EMD: CHT (*tube rendering*) in molecular complexation with EC (stick rendering); (**b**) WMD molecular complex consisting of GEL (*yellow secondary structure*), PVA (*ball-and-cylinder rendering*), HEC (*tube rendering*), and PAA (*stick rendering*); and (**c**) PCMS molecular complex, after molecular simulations in vacuum. Color coded molecular structure of (**d**) EMD; (**e**) WMD; and (**f**) PCMS for easy identification of the molecular architecture. Solvent accessible molecular surfaces in translucent mode corresponding to (**g**) EMD; (**h**) WMD; and (**i**) PCMS. Standard element color codes: C (*cyan*), O (*red*), H (*white*), and N (*blue*). Molecule color codes: CHT (*yellow*), EC (*violet*), GEL (*brown*), PVA (*red*), PAA (*blue*), HEC (*green*). Secondary structure of GEL is shown in *yellow tube rendering*.

stabilization in the energy profile of the bipolymeric EMD can be attributed to the non-bonding energy components – van der Waal's forces and electrostatic contributions. Geometrically, the formation of EMD was strengthened by both inter- and intra-molecular bonding comprising of –NH…OH- (CHT-CHT) and –NH…C-O-C (CHT-EC) H-bonds (Fig. 12a and d).

$$E_{GEL} = 17.160\ V_{\sum} = 0.769\ V_b + 17.418\ V_\theta + 15.777\ V_\varphi - 1.503\ V_{ij} - 0.429\ V_{hb} - 14.870\ V_{el} \quad (12)$$

$$E_{HEC} = 17.765\ V_{\sum} = 1.704\ V_b + 12.709\ V_\theta + 12.532\ V_\varphi + 5.913\ V_{ij} - 0.944\ V_{hb} - 14.148\ V_{el} \quad (13)$$

$$E_{PAA} = 5.661\ V_{\sum} = 1.099\ V_b + 4.981\ V_\theta + 2.547\ V_\varphi - 2.852\ V_{ij} - 0.114\ V_{hb} \quad (14)$$

$$E_{PVA} = 5.173\ V_{\sum} = 0.615\ V_b + 1.652\ V_\theta + 0.881\ V_\varphi + 4.895\ V_{ij} - 2.871\ V_{hb} \quad (15)$$

$$E_{WMD} = 4.627\ V_{\sum} = 3.985\ V_b + 37.300\ V_\theta + 33.331\ V_\varphi - 32.879\ V_{ij} - 4.368\ V_{hb} - 32.742\ V_{el}; \Delta E = -45.759\ \text{kcal/mol} \quad (16)$$

The formulation and formation of water-based multi-elemental dispersion (WMD) presented a complex modeling paradigm with sequential reactional profiling achieved through step-by-step addition of polymeric components. The finalized tetrapolymeric PVA-PAA-HEC-GEL archetype is shown in Fig. 12b and e and the formation of a loosely interconnected polymeric network is evident from the partial intermolecular H-bonding involving HEC-PVA (O-H…C-O-C) and PAA-GEL (C = O…N-H). The finalized energy terms, however, confirmed the formation of a favourable polymeric complex with a –ve free energy of binding (ΔE = −45.759 kcal/mol) wherein the major contributors were the non-bonding hydrophobic interactions (van der Waals forces) accounting for 80% of the total interaction energy.

$$E_{PCMS} = 8.425\ V_{\sum} = 7.420\ V_b + 64.021\ V_\theta + 62.107\ V_\varphi - 39.277\ V_{ij} - 3.480\ V_{hb} - 82.365\ V_{el}; \Delta E = -100.054 \text{kcal/mol} \quad (17)$$

The finalized multipolymeric platform – PCMS – consisted of co-blended ethanolic and aqueous dispersions and hence was even more complicated architecture as compared to its bi- and tetra-polymeric components. Interestingly, the partial bonding interactions observed in EMD and WMD provided a perfect rationale for the above mentioned co-blending as the finalized EMD-WMD (Fig. 12c and f) displayed extensive hydrogen bonding interactions involving GEL-PAA, EC-PVA, EC-CHT, CHT-HEC, and HEC-PAA leading to the formation of a well-connected polymeric network. However, no polyelectrolyte formation between CHT and PAA was observed which can be attributed to the steric hindrance caused by the multi-component character of PCMS. Correspondingly, the final optimized energy for the hexa-polymeric EMD-WMD complex displayed a –ve stabilization energy of ≈100 kcal/mol—much higher than the individual components. More importantly, the energy stabilization can be attributed to both bonding as well as non-bonding interaction energies wherein the bonding contributions—bond, angle and torsional energies—provided much need geometrical adjustments for the sustained release performance of the PCMS. The solvent accessible 3days-geometrical surfaces generated for EMD, WMD, and PCMS (Fig. 12g–i) further demonstrate that the PCMS provided a better distribution of solid and porous volumes inside the matrix structure as compared to EMD and WMD—hence proving the porosity modulated performance behavior of PCMS. The unique stabilized

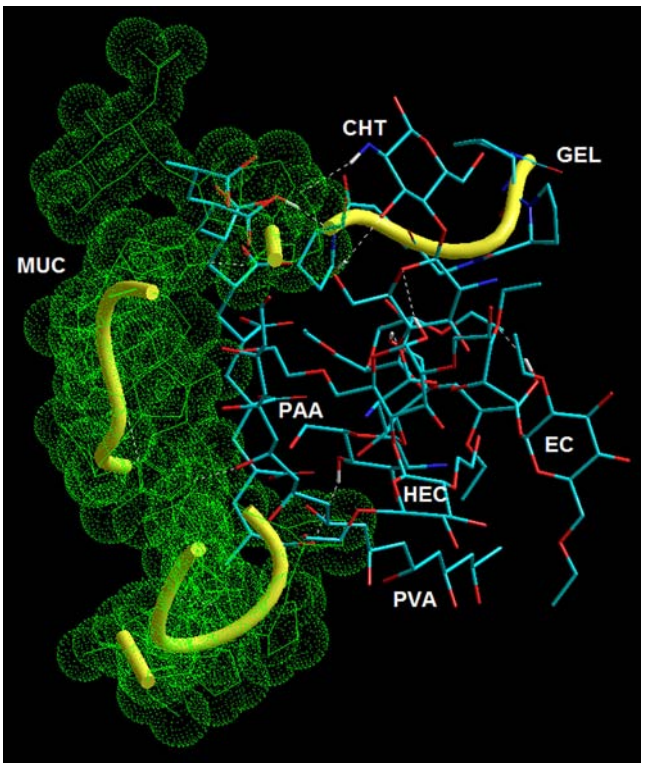

Fig. 13 Visualization of geometrical preferences of PCMS (CHT, EC, PVA, PAA, HEC, and GEL) in complexation with MUC, after molecular simulations in vacuum. Color codes for HPMC and EUD: C (*cyan*), O (*red*), H (*white*), and P (*yellow*). Standard element color codes: C (*cyan*), O (*red*), H (*white*), and N (*blue*). Molecule color codes: MUC (*green*). Secondary structure of MUC and GEL is shown in *yellow tube rendering*.

geometry corresponding to the solvent accessible area, torsional constraints, and matrix distribution described above may explain the abovementioned relationship between matrix hydration, porous structure configuration and physicomechanical textural transitions.

Muco-Adhesivity of PCMS Configuration

To ascertain the mucoadhesion mechanism of PCMS, the finally optimized EMD-WMD molecular complex was modeled with a glycosylated mucin derivative (MUC). As evident from Eqs. 17–19, the MUC-PCMS interaction was stabilized by a binding energy of −73.268 kcal/mol with the non-bonding interactions – van der Waals forces (≈−55 kcal/mol), and electrostatic interactions (≈−25 kcal/mol) - playing a major role in *in silico* mucoadhesion. A close observation of Fig. 13 reveals that chitosan (CHT) and Carbopol 974P NF (PAA) demonstrated H-bonding with the MUC molecule. The non-formation of CHT-PAA polyelectrolyte complex in PCMS further assisted in the availability of these molecules for mucoadhesion. Additionally, the involvement of atleast one component each from EMD and WMD in mucoadhesion confirms the importance of combining EMD and WMD components to obtain the PCMS configuration.

$$E_{MUC} = -166.812\ \ V_{\sum} = 5.474\ \ V_b + 70.351\ \ V_\theta + 55.173\ \ V_\varphi - 29.066\ \ V_{ij} - 7.096\ \ V_{hb} - 261.649\ \ V_{el} \quad (18)$$

$$E_{MUC-PCMS} = -231.655\ \ V_{\sum} = 13.735\ \ V_b + 151.349\ \ V_\theta + 115.696\ \ V_\varphi - 126.563\ \ V_{ij} - 11.270\ \ V_{hb} - 374.602\ \ V_{el}; \quad (19)$$

$$\Delta E = -73.268 \text{kcal/mol}$$

CONCLUSIONS

The high performance Box-Behnken experimental design was statistically and mathematically efficient in developing, evaluating and optimizing the novel PCMS formulations. This quadratic design as well as polynomial mathematical equations exposed the significant ($p \leq 0.05$) direct or indirect ($R^2 values = - or +$) controlling impact of measures of porosity investigated in this study (average pore diameter and cumulative surface area of pores) on the magnitude of relevant physicochemical and physicomechanical properties (mean dissolution time, mucoadhesion, matrix resilience, viscosity, *ex vivo* permeation and drug loading capacity) which impacted the overall performance of the PCMS. Additionally, the potential mechanisms guiding the construction and function of the optimized PCMS were elucidated and validated utilizing experimental and computational processes respectively. The experimental approach revealed that the methodical phases executed during the manufacture of the PCMS were based on structurally non-destructive physical and mechanical procedural transitions and that the overall performance of the formulation was due to the combinative properties of the employed excipients. Furthermore, the mechanism of action of the PCMS was associated with the disruption of its specifically ordered porous structure by physical processes such as extrication, distension, plasticization and dissolution due to aqueous medium diffusion capabilities. These processes also had significant impacts on the quality of the PCMS physicomechanical texture but retained its fundamental chemical nature as hydration progressed. Furthermore, the outcome of the *in silico* analysis correlated and verified the findings of the *in vitro* and *ex vivo* experimental procedures. Overall, the preparation and performance of the PCMS was successfully mechanistically established and outcomes can be beneficial for investigating similar porosity-dependent formulations. The outcomes realized from this extensive investigation can be extrapolated and applied to the elucidation of the controlling/underlying mechanisms of other polymer-based, porosity-controlled drug delivery systems.

ACKNOWLEDGMENTS AND DISCLOSURES

This project was funded by the National Research Foundation (NRF) of South Africa.

The Authors confirm that there are no conflicts of interest.

REFERENCES

1. Mehta KA, Kislalioglu MS, Phuapradit W, Malick AW, Shah NH. Effect of formulation and process variables on porosity parameters and release rates from a multi-unit erosion matrix of a poorly soluble drug. J Control Release. 2000;63(1–2):201–11.
2. Popovici RF, Seftel EM, Mihai GD, Popovici E, Voicu VA. Controlled drug delivery system based on ordered mesoporous silica matrices of captopril as Angiotensin-Converting Enzyme inhibitor drug. J Pharm Sci. 2011;100(2):704–14.
3. Tai H, Mather ML, Howard D, Wang W, White LJ, Crowe JA, *et al.* Control of pore size and structure of tissue engineering scaffolds produced by supercritical fluid processing. Eur Cells Mater. 2007;14:64–77.
4. Ginty PJ, Barry JJA, White LJ, Howdle SM, Shakesheff KM. Controlling protein release from scaffolds using polymer blends and composite. Eur J Pharm Biopharm. 2008;68(1):82–9.
5. Grinberg O, Binderman I, Bahar H, Ziberman M. Highly porous bioresorbable scaffolds with controlled release of bioactive agents for tissue-regeneration applications. Acta Biomaterial. 2010;6(4):1278–87.
6. Hawkins AM, Milbrandt TA, Puleo DA, Hilt JZ. Composite hydrogel scaffolds with controlled pore opening via biodegradable hydrogel porogen degradation. J Biomed Mater Res A. 2014;102(2):400–12.
7. Qi X-N, Mou Z-L, Zhang J, Zhang Z-Q. Preparation of chitosan/silk fibroin/hydroxyapatite porous scaffold and its characteristics in

comparison to bi-component scaffolds. J Biomed Mater Res A. 2014;102(2):366–72.
8. Aerts CA, Veeraedt E, Depla A, Follens L, Froyen L, Van Humbeeck J, *et al.* Potential of amorphous microporous silica for ibuprofen controlled release. Int J Pharm. 2010;397(1–2):84–91.
9. Makhija SN, Vavia PR. Controlled porosity osmotic pump-based controlled release systems of pseudoephedrine. I. Cellulose acetate as a semi-permeable membrane. J Control Release. 2003;89(1):5–18.
10. Liu H, Yang X-G, Nie S-F, Wei L-L, Zhou L-L, Liu H, *et al.* Chitosan-based controlled porosity osmotic pump for colon-specific delivery system: Screening of formulation variables and *in vitro* investigation. Int J Pharm. 2007;332(1–2):115–24.
11. Kumaravelrajan R, Narayanan N, Suba V. Development and evaluation of controlled porosity osmotic pump for Nifedipine and Metoprolol combination. Lipids Health Dis. 2011;10(51):1–13.
12. Adibkia K, Ghanbarzadeh S, Shokri MH, Arami Z, Arash Z, Shokri JT. Micro-porous surfaces in controlled drug delivery systems: design and evaluation of diltiazem hydrochloride controlled porosity osmotic pump using non-ionic surfactants as pore-former. Pharm Dev Technol. 2014;19(4):507–12.
13. Lin WJ, Lee HK, Wang DM. The influence of plasticizers on the release of theophylline from microporous-controlled tablets. J Control Release. 2004;99(3):415–21.
14. Mishira M, Mishira B. Design and evaluation of microporous membrane coated matrix tablets for a highly water soluble drug. Chem Pharm Bull. 2010;58(7):995–1000.
15. Park HS, Kim CW, Lee HJ, Choi JH, Lee SG, Yun Y-P, *et al.* A mesoporous silica nanoparticle with charge-convertible pore walls for efficient intracellular protein delivery. Nanotechnology. 2010;21(22):1–9.
16. Zhang Y, Zhi Z, Jiang T, Zhang J, Wang Z, Wang S. Spherical mesoporous silica nanoparticles for loading and release of poorly water-soluble drug telmisartan. J Control Release. 2010;145(3):257–63.
17. Yang Y-J, Tao X, Hou Q, Chen J-F. Fluorescent mesoporous silica nanotubes incorporating CdS quantum dots for controlled release of ibuprofen. Acta Biomater. 2009;5(9):3488–96.
18. Kim MS, Seo KS, Hyun H, Kim SK, Khang G, Lee HB. Sustained release of bovine serum albumin using implantable wafers prepared by MPEG-PLGA diblock copolymers. Int J Pharm. 2005;304(1–2):165–77.
19. Verraedt E, Braem A, Chaudhari A, Thevissen K, Adams E, Van Mellasrt L, *et al.* Controlled release of chlorhexidine antiseptic from microporous amorphous silica applied in open porosity of an implant surface. Int J Pharm. 2011;419(1–2):28–32.
20. Espanol M, Perez RA, Montufar EB, Marichal C, Sacco A, Ginebra WP. Intrinsic porosity of calcium phosphate cements and its significance for drug delivery and tissue engineering applications. Acta Biomater. 2009;5(7):2752–62.
21. Hong M-H, Son J-S, Kim K-M, Han M, Oh DS, Lee Y-K. Drug-loaded porous spherical hydroxyapatite granules for bone regeneration. J Mater Sci-Mater M. 2011;22(2):349–55.
22. Sotthivirat S, Haslam JL, Lee PI, Rao VM, Stella VJ. Release mechanisms of a sparingly water-soluble drug from controlled porosity-osmotic pump pellets using Sulfobutylether-β-Cyclodextrin as both a solubilizing and osmotic agent. J Pharm Sci. 2009;98(6):1992–2000.
23. Ilyas S, Gal S. Optical devices from porous silicon having continuously varying refractive index. J Mater Sci-Mater El. 2007;18:S61–4.
24. Webb PA, Orr C. Analytical methods in fine particle technology. Texas: Norcross, Micromeritics Instrument Corporation; 1997.
25. Adeleke OA, Pillay V, du Toit LC, Choonara YE. Construction and *in vitro* characterization of an optimized porosity-enabled amalgamated matrix for sustained transbuccal drug delivery. Int J Pharm. 2010;391(1–2):79–89.
26. Aguilar-de-Leyva A, Cifuentes C, Rajabi-Siahboomi AR, Caraballo I. Study of the critical points and the role of pores and viscosity in carbamazepine hydrophilic matrix tablets. Eur J Pharm Biopharm. 2012;80(1):136–42.
27. Sher P, Ingavle G, Ponrathnam S, Poddar P, Pawar AP. Modulation and optimization of drug release from uncoated low density porous carrier based delivery system. AAPS PharmSciTech. 2009;10(2):547–58.
28. Hoa MLK, Lu M, Zhang Y. Preparations of porous materials with ordered hole structure. Adv Colloid Interfac. 2006;121(1–3):9–23.
29. Yu H-D, Tee SY, Han M-Y. Preparation of porosity-controlled calcium carbonate by thermal decomposition of volume content-variable calcium carboxylate derivatives. Chem Commun. 2013;49(39):4229–31.
30. Sudhakar Y, Kuotsu K, Bandyopadhyay AK. Buccal bioadhesive drug delivery- a promising option for orally less efficient drugs. J Control Release. 2006;114(1):15–40.
31. Smart JD. The basics and underlying mechanisms of mucoadhesion. Adv Drug Deliver Rev. 2005;57(11):1556–68.
32. Peh KK, Wong CF. Polymeric films as vehicle for buccal delivery: swelling, mechanical and bioadhesive properties. J Pharm Sci. 1999;2(2):53–61.
33. Pillay V, Fassihi R. Evaluation and comparison of dissolution data derived from different modified release dosage forms: An alternative method. J Control Release. 1998;55(1):45–55.
34. Ansari M, Kazemipour M, Talebria J. The development and validation of a dissolution method for clomipramine solid dosage forms. Dissol Technol. 2004;August:16–24.
35. Van Eyk AD, der Bijl V. Comparative permeability of various chemical markers through human vaginal and buccal mucosa as well as porcine buccal and mouth floor mucosa. Arch Oral Biol. 2004;49(5):387–92.
36. Giannola LI, De Caro V, Giandalia G, Siragusa MG, Tripodo C, Florena AM, *et al.* Release of naltrexone on buccal mucosa: Permeation studies, histological aspects and matrix system design. Eur J Pharm Biopharm. 2007;67(2):425–33.
37. Minghetti P, Cilurzo F, Casiraghi A, Montanari L, Fini A. *Ex vivo* study of transdermal permeation of four diclofenac salts from different vehicles. J Pharm Sci. 2007;96(4):814–23.
38. Kolawole OA, Pillay V, Choonara YE. Novel polyamide 6,10 variants synthesized by modified interfacial polymerization for application as a rate-modulated monolithic drug delivery system. J Bioact Compat Pol. 2007;22(3):281–313.
39. Kumar P, Pillay V, Choonara YE, Modi G, Naidoo D, du Toit LC. In silico theoretical molecular modeling for Alzheimer's disease: The nicotine-Curcumin paradigm in neuroprotection and neurotherapy. Int J Mol Sci. 2011;12:694–724.
40. Silverstein RM, Bassler GC, Morril TC. Spectrometric identification of organic compounds. New York: Wiley; 1991.
41. Taylor LS, Zografi G. Spectroscopic characterization of interactions between PVP and indomethacin in amorphous molecular dispersions. Pharm Res. 1997;14(12):1691–8.
42. Sethia S, Squillante E. Solid dispersions of carbamazepine in PVP K30 by conventional solvent evaporation and supercritical methods. Int J Pharm. 2004;272(1–2):1–10.
43. Yu BY, Chung JW, Kwak SY. Reduced Migration from Flexible Poly(vinyl chloride) of a Plasticizer Containing β-Cyclodextrin Derivative. Environ Sci Technol. 2008;42:7522–7.